STRAIN HARDENING AND ANISOTROPIC BEHAVIOR OF ALUMINUM ALLOY 5182 SUBJECT TO PREFORM ANNEALING

A thesis submitted to the graduate division of
The University of Hawaiʻi at Mānoa in partial fulfillment
of the requirements for the degree of

Master of Science
in
Mechanical Engineering
December 2013

By

Bonan Zhou

Thesis Committee:

Jingjing Li, Chairperson

Scott F. Miller

John E Carsley, General Motors

ACKNOWLEDGEMENTS

I would like to thank my advisor, committee members, and collaborators for all their guidance and support. This work is indebted to the counsel of my advisor, Professor Jingjing Li, who helped me become a much better researcher with her words of wisdom, encouragement, and occasionally, constructive disapproval.

I wish to express my gratitude to Dr. Blair Carlson, laboratory group manager at General Motors Research and Development, and Drs. John Carsley, Thomas Stoughton, and Lou Hector Jr., for their support and invaluable input at General Motors Research and Development. I would like to thank the technical staff at GM, Todd Meitzner, Keith Snavely, Willie Dixon, and Joshua Lasceski for their help conducting the experiments that were critical to this research.

Lastly, I would also like to thank my fellow visiting research interns at General Motors, Simon Hall and Paul Janiak for the lunchtime discussions on engineering, Kaifeng Wang for his training in experimental technique and especially Junying Min for EBSD analysis.

ABSTRACT

STRAIN HARDENING AND ANISOTROPIC BEHAVIOR OF ALUMINUM ALLOY 5182 SUBJECT TO PREFORM ANNEALING

By

Bonan (Julian) Zhou

Chair: Jingjing Li

Two essential elements of formability analysis are accurate strain-hardening laws and knowledge of material anisotropy, captured by the R-value parameter. Refinement of both of these areas will further enable the incorporation of lightweight materials, such as aluminum alloy 5182-O in automobiles, despite their traditionally lower formability than mild steel sheet. Therefore, improved modeling of strain-hardening with focus on high-strain deformation and R-value analysis is introduced in this research with experimental validation.

Table of Contents

CHAPTER 1

INTRODUCTION

1.1 MOTIVATION

The automobile industry is actively looking for solutions to reduce vehicle weight in order to improve fuel economy while meeting all safety requirements. Aluminum alloys are good substitutes for steels in many applications to save mass and can afford a weight savings of up to 55% compared to an equivalent steel structure with a lifetime fuel savings of 500 - 700 gallons of gasoline, while meeting or exceeding crashworthiness standards of similar sized steel structures [Aluminum Autodesign Review, 1998]. The other advantages include recyclability, one-third the mass density of steel, and the ability to meet torsion and stiffness requirements.

One of the biggest challenges for implementing aluminum sheet applications is its lower formability compared to conventional steels. For example, automotive aluminum alloys, such as 5xxx and 6xxx, often tear or break if they are stamped using the same die geometry that was designed for steel sheets. Tensile elongation of aluminum alloys at room temperature is generally lower than 30% [Aluminum Autodesign Review, 1998], while the elongation of commercial steel is approximately 40% [U. S. Steel, 2011].

A promising technique called 'preform annealing' [Krajewski, 2007] was developed to address this challenge through a multi-stage forming and intermediate annealing process. There are two forming stages and one annealing stage in this process. During the process, aluminum sheet is partially stamped to a 'preform' shape in the 1st forming stage, followed by a rapid anneal on the highly pre-strained portions of the preform panel, which is finally stamped to the desired shape in a 2nd forming stage as illustrated in

Figure 1.1. This technique can improve the formability of Al alloys by introducing annealing that partially (or entirely) removes the effects of cold work from the preform; and it has been demonstrated in the forming of a one-piece aluminum inner door panel using convection heating in the laboratory [Lee, et al., 2006].

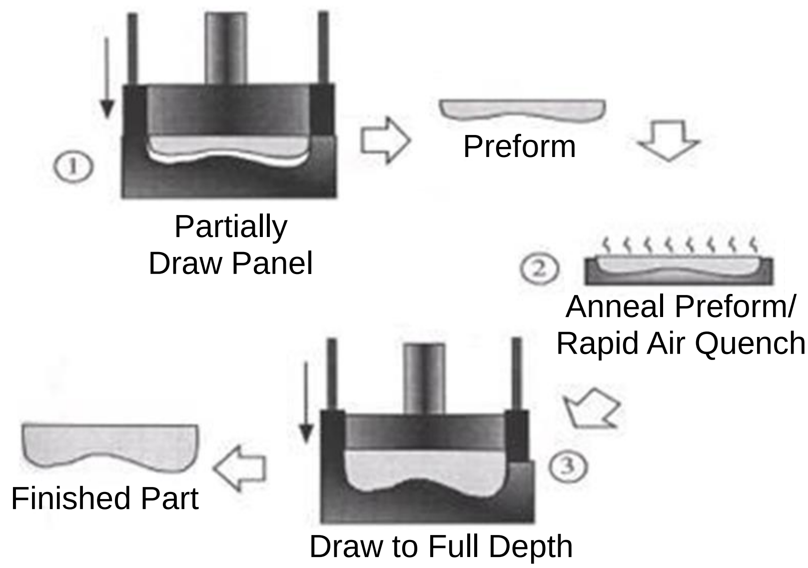

Figure 1.1 The preform annealing process [Lee, et al., 2006]

Preform annealing has been investigated on non-heat treatable and heat treatable aluminum alloys. Li et al. [2011a, 2011b, 2013] and Tatiparti et al. [2013] have studied how preform annealing influences the kinetic behavior, forming limit microstructure and texture of a non-heat treatable aluminum alloy 5182. Wang et al. [2014a-c] have analyzed the tensile behavior, anisotropic property and forming limit criterion of a heat treatable aluminum AAx610-T4PD under the preform annealing process. The research on both non-heat treatable and heat treatable aluminum alloys has shown that the preform annealing technology can significantly improve the formability of the aluminum alloys, but indeed change the material microstructure and mechanical properties.

For this new forming technology, the fundamental research on how pre-strain and annealing conditions affect the plastic and anisotropic behavior of the addressed alloy (AA5182-O) for the 2nd forming stage is limited and current material models do not accurately capture those changes. Accurate material models are the key factors for proper finite element analysis, failure prediction and thus manufacturing process design. Compared to conventional one step forming, the complexity of this two-stage forming with intermediate annealing process increases the difficulty of accurate modeling.

Material models enable significantly accurate finite element analysis, failure prediction and thus manufacturing process design. A number of works have investigated strain path and strain path changes on strain hardening behavior in aluminum alloy sheets based on Voce, Swift or Power law [Wilson~~,~~ et al., 1990; Juul Jensen and Hansen, 1990; Yoon~~,~~ et al., 2005]; however, two problems still exist: 1) none of current strain hardening models has adequate accuracy to describe the strain hardening behavior of aluminum over a large strain range including the region of diffuse necking. The Swift and Power laws over-predict the stress, while the Voce law saturates and under-predicts the actual hardening behavior at large strains. 2) When an annealing heat treatment is applied to pre-strained material, the combined effects from cold work and annealing on the strain-hardening model are unknown.

Furthermore, anisotropy significantly influences the strain distribution in sheet metal forming, and is characterized by measurement of the plastic strain ratio, R-value. As an important input to the yield function, R-values show considerable variations along different orientations, and could be changed by non-monotonic and non-proportional loading paths [Zamiri and Pourboghrat, 2007]. Limited studies have been conducted to give a comprehensive view of the combined effects of pre-strain and annealing on the R-values. This leads to a dearth of fundamental science and understanding of sheet metal anisotropy and its relationship between process history (i.e. pre-strain and annealing) and material crystallographic texture and microstructural evolution.

1.2 RESEARCH OBJECTIVES

The objective of this research is to characterize and model the plastic behavior of AA5182-O in a multi-stage forming and annealing process and to create accurate material models that account for pre-strain and annealing effects. The specific tasks are:

1) To record tensile behavior for a large strain range (post-diffuse necking) through high-speed digital image correlation techniques for specimens with various histories of pre-strain and annealing conditions;

2) To model flow behavior by combining experimental and statistical methods to create accurate strain hardening models for aluminum alloy;

3) To analyze and model anisotropic behavior of aluminum sheet and its interaction with pre-strain and annealing history.

As expected, the results of this research will advance the preform annealing technique as well as traditional stamping techniques of forming complex aluminum shapes through material characterization and modeling. The results will enhance the understanding of the deformation mechanisms of aluminum alloys and make contributions to experimental technique and mechanics theory.

1.3 ORGANIZATION OF DISSERTATION

This dissertation is presented in a multiple manuscript format. Chapters 2 and 3 are written as individual research papers that are partially revised for this dissertation and include abstract, main body section and references.

Chapter 2 presents a new strain-hardening model with emphasis on the characterization of the localized neck with experimental data.

Chapter 3 presents a new concept of "strain path angle" to view the anisotropy evaluation in the specimen coordinate system subjected to different pre-strain and annealing histories.

Chapter 4 summarizes the investigation and proposes future work.

REFERENCES

Aluminum Autodesign Review, (1998), The aluminum Society, 6 (3).

Krajewski, P. E., (2007), “Method for production of stamped sheet metal panels,” US Patent 7,260,972, B2.

Juul Jensen, D., Hansen, N., “Flow stress anisotropy in aluminum,” Acta Metall. Mater. 38, 1369–1380 (1990).

Lee, T. M., Hartfield-Wünsch, S. E., Xu, S., (2006), “Demonstration of the preform anneal process to form a one-piece aluminum door inner panel,” SAE, 2006-01-0987

Li, J. J., Kim, S., Lee, T. M., Krajewski, P. E., Wang, H., Hu, S. J., (2011a), “The effect of pre-strain and subsequent annealing on the mechanical behavior of AA5182-O,” Materials Science and Engineering A, 582, 3905-3914

Li, J. J., Hu, S. J., Carsley, J. E., Lee, T. M., Hector, Jr., L. G., Mishra, S., (2011b), “Postanneal Mechanical Properties of Pre-strained AA5182-O Sheets,” ASME Journal of Manufacturing Science and Engineering, 133, 061007-1-10.

Li, J. J., Carsley, J. E., Stoughton, T. B., Hector, Jr., L. G., Hu, S. J., (2013), “Forming Limit Analysis for Two-Stage Forming with Intermediate Annealing,” International Journal of Plasticity, 45, 21-43.

Mishra, S.K., Tatiparti, S.S.V., Tiwari, S.M., Raghavan, R.S., Carsley, J.E., Li, J.J., (2013), “Annealing Behavior of Aluminum Alloy 5182 Deformed in Plane Strain and Equibiaxial Strain Paths,” Philosophical Magazine, 93, 2613-2629.

U. S. Steel, (2011), “Commercial Steel (CS) Type B,” 8 August 2011, <http://www.ussteel.com/corp/auto/tech/grades/lowcarbon/cs_type_b.asp>.

Wang, K., Carsley, J. E., Zhang, L., Li, J. J., He., B., (2014a), “Measuring forming limit strains with digital image correlation analysis,” Journal of Materials Processing Technology, under review.

Wang, K., Carsley, J. E., Zhang, L., Stoughton, T. B., Li, J. J., Carlson, B.E., (2014b), “Forming limits of an age hardenable aluminum sheet after pre-straining and annealing,” International Journal of Mechanical Sciences, under review.

Wang, K., He, B., Carsley, J. E., Raghavan, R.S., Hartfield-Wünsch, S.E., Li, J., (2014c), “Preform annealing age hardenable aluminum: property-structure characterization,” Materials Science and Engineering A, accepted.

Wilson, D.V., Zandrahimi, M., Roberts, W.T., (1990), “Effects of changes in strain path on work-hardening in CP aluminum and an Al–Cu–Mg–Si alloy,” Acta Metall. Mater. 38, 215–226.

Yoon, J. W., Barlat, F., Gracio, J. J., Rauch, E., (2005), “Anisotropic strain hardening behavior in simple shear for cube textured aluminum alloy sheets,” Int. J. Plasticity 21, 2426-2447.

Zamiri, A., Pourboghrat, F., (2007), “Characterization and development of an evolutionary yield function for the superconducting niobium sheet,” Int. J. Solids. Struct. 44, 8627-8647.

CHAPTER 2

STRAIN HARDENING BEHAVIOR OF ALUMINUM ALLOY 5182 SUBJECT TO PREFORM ANNEALING

ABSTRACT

A new strain-hardening model was proposed and compared with existing models to characterize high-strain plasticity behavior of aluminum alloy 5182-O. This model modifies the Voce law by introducing a linear hardening term that begins at the instant the localized neck is formed. This term represents the tangent to the Voce law which bounds the true stress-strain curve along with the Voce law, so that an empirical weighting parameter can be used to more accurately predict the true stress state. This model was compared statistically with other strain-hardening laws and weighting methods and found to be robust at high strains for the AA5182 subjected to a variety of different pre-strains and annealing conditions.

2.1 INTRODUCTION

To broaden the implementation of aluminum alloys in the transportation sector for light weight vehicles, a two-stage forming with annealing method, called "perform annealing" [Krajewski, 2007] was proposed for improving the formability of aluminum alloys. During this process, the aluminum alloy is first deformed to a certain level (i.e. preform), followed by a rapid annealing to partially or entirely remove the effects of work hardening caused by the preform step; after this, it is deformed to the desired shape in the 2^{nd}-stage of forming. To understand the formability of a material, or its ability to be deformed into some desired shape, it is helpful to mathematically represent the stress that the material experiences as a function of the strain it has undergone. During forming processes, for instance, knowing this stress-strain curve facilitates prediction of the degree to which a material can be deformed without fracturing and the load required for the deformation. However, minimal attention has been directed at developing the strain-hardening model for this forming process where the strain-path changes and annealing (heat treatment) are included.

As the relationship between true stress and true plastic strain is generally represented empirically, there are several models that are used to quantify this relationship that vary across materials. Three common, well established models used for metals are the Hollomon [1945], Swift [1952] and Voce equations [Voce, 1955]. In general, the strain hardening models are grouped into two types: ‘‘saturation” or ‘‘Voce” models, where the stresses saturate at large strains (e.g. Brown-Anand model [Anand, 1982, 1985; Brown et al., 1989], such as the modified Bodner-Partom model [(Bodner and Partom, 1975; Chen et al., 2008], MTS model [Kocks, 1976; Mecking and Kocks, 1981; Follansbee and Kocks, 1988], and Lin-Wagoner model [Lin and Wagoner, 1987]) and ‘‘Hollomon” or ‘‘power-law” models, where the stresses are unbounded at large strains (e.g. Zirilli–Armstrong model [Zerilli and Ronald, 1987], Rusinek–Klepaczko model [(Klepaczko, 1987; Rusinek and Klepaczko, 2001; Rusinek et al., 2007], and the Khan–Huang–Liang model [Khan and Huang, 1992; Khan and Liang, 1999; Khan et al., 2004]). The saturation-type models are more suitable for face centered cubic (FCC) metals, such as aluminum [Butec et al., 2003 and Jain et al., 1996], while the power-law-type models are more suitable for body-centered cubic (BCC) metal, for instance the steel alloys [Johnson and Holmquist, 1988].

The difficultly in improving strain hardening laws is that they are by nature empirical; therefore, it is not easy to explain why some models work better for certain metals under certain conditions than other models based solely on theoretical considerations [Kleemola, 1974]. It has been experimentally observed that the Voce law used to model aluminum begins to deviate from the experimental stress-strain curve at large strains, under-predicting the known stress values whereas the Hollomon law over-predicts these stresses. Therefore, a model bounded between these two laws may be more appropriate for aluminum alloys. A “H/V” model has been recently developed by weighting Voce and Hollomon laws for some dual phase (DP) steels [Sung et al., 2010]. Another difficulty in improving strain hardening laws particularly for Al-Mg alloys is the occurrence of Portevin-Le Chatelier (PLC) bands (a phenomenon associated with the dynamic strain aging and Mg solute depinning of dislocations [Hähner, 1996a,b]), which cause the repeated serrations in stress-strain curves and makes curve fitting difficult. The robustness of strain hardening models also varies significantly with process conditions, such as changes in temperature, strain-path, or direction of straining [Sing, 1997]. It is important to mathematically improve the robustness of these models in the face of common sheet metal forming steps, such as strain-path changes, particularly for two-stage forming with annealing. Thus, an additional consideration in this research when accounting for strain path changes and annealing treatments is to focus on the robustness of the stress-strain equations at these high strains, where the material is near fracture.

An approach to correcting the under-prediction of these stress-strain curves at high strains is to note that the actual stress response to strain saturates, meaning that its rate of increase decays. Thus, for any empirical model considered, it ought to be true that the tangent to this function at the point of deviation should serve as an upper bound to all of the stress data after this point [Ling, 1996]. Therefore, a new model is considered in this research, where the traditional Voce law is used to model the stress-strain behavior up to the point of deviation, at which point the tangent to the Voce law is then constructed and used to correct the Voce law through a weighted averaging procedure. The effectiveness of this method is then statistically monitored and compared to other known methods~~,~~ as the material is subjected to different process conditions, such altering the direction of straining and annealing treatments.

2.2 STRESS-STRAIN RELATION FUNDAMENTALS

In plastic deformation, ductile metals react to the imposed strains by developing progressively greater internal stresses reflecting the increased difficulty of dislocation motion, a phenomenon called “cold work hardening” or “strain hardening.” This stress reaction to strain characterizes the plastic behavior of the metal and is described quantitatively for a given model of strain by the flow curve. In this research, a new stress-strain model is proposed and compared to the existing documented models.

Model I: Voce model [Voce, 1955]

An exponential form of hardening was proposed for materials that exhibit a saturated isotropic hardening under monotonic loading. It is defined as follows:

$$\sigma = A + Be^{C\varepsilon} \tag{2.1}$$

where *A*, *B*, and *C* are empirically determined parameters and σ and ε are the true stress and true strain, respectively.

Model II: Hollomon Model (Power law [1945])

Often strain hardening is represented by the Hollomon law, described by

$$\sigma = K\varepsilon^{n} \tag{2.2}$$

where K is the strength coefficient and n is the strain hardening exponent.

<u>Model III Hollomon-Voce model [Sung, et al., 2010]</u>

It is generally agreed that the Hollomon law is not a particularly good representation for Al alloys. For Al alloys, the Hollomon law tends to over-predict the actual stress, while the Voce law saturates and predicts lower than the actual stress at large strains. Therefore, the Hollomon law serves as an upper bound, while the Voce law serves as a lower bound [Sung, et al., 2010]. In so doing, a weighting parameter (α) can be empirically determined to combine these two functions with rule-of-mixtures approach defined as follows:

$$\sigma = \alpha(A + Be^{C\varepsilon}) + (1-\alpha)K\varepsilon^{n} \tag{2.3}$$

<u>Model IV: Voce-Linear model [Tome et al., 1984]</u>

The fourth model considered was the Voce-Linear model, which is a modification of the Voce law allowing for an asymptotic hardening rate at large strain:

$$\sigma = A' + B'e^{C'\varepsilon} + D'\varepsilon \tag{2.4}$$

where A', B', C' and D' are the fitting parameters for the flow curve.

<u>Model V: Voce-Tangent model</u>

The fifth is a newly proposed model, the Voce-Tangent model, in which the fitting is a pure the Voce law up to the point at which necking occurs. Thereafter, the data is bounded between the pure Voce law and the tangent evaluated at the onset of necking. Thus, like the Voce-Linear model, a linear term is mixed with the Voce law using an empirically determined weighting parameter (w), the key difference being that this mixture does not apply until after necking. This is defined as follows:

$$\sigma = \begin{cases} A + Be^{C\varepsilon}, \ \varepsilon \leq \ \varepsilon_n \\ w(A + Be^{C\varepsilon}) + (1 - w)\left((\varepsilon - \varepsilon_n) \cdot \frac{d\sigma}{d\varepsilon}\Big|_{\varepsilon=\varepsilon_n} + \ \sigma(\varepsilon_n)\right), \ \varepsilon > \ \varepsilon_n \end{cases} \quad (2.5)$$

where ε_n and $\sigma(\varepsilon_n)$ are the true strain and true stress evaluated at necking; $\frac{d\sigma}{d\varepsilon}\Big|_{\varepsilon=\varepsilon_n}$ is the slope of the tangent evaluated at the instant of necking; A, B, and C are the Voce parameters, described in Eq. (2.1). This step model separates the flow behavior into two zones—before and after necking, in which the Voce model fits the stress data before necking and the weighted mixture of the Voce and tangent components fit the stress data after necking.

2.3 MATERIALS, EXPERIMENTAL AND MODELING PROCEDURE

The experiment focuses on tensile tests after pre-straining and annealing to examine the correlation between process variables and flow behavior. Digital image correlation (DIC) was used to measure strains including the large strains in the neck, which is not possible with conventional extensometers.

2.3.1. Material

AA5182-O with 1.1 mm nominal thickness and chemical composition (wt%) of Al-4.3Mg0.34Mn-0.21Fe-0.03Si was used in the experiment. The as-received material properties tested from previous work [Li et al., 2011] are summarized in Table 1 as a reference.

Table 2.1: Typical room-temperature mechanical properties of AA5182-O, as-received [Li et al., 2011]

Young's modulus (GPa)	Yield stress (MPa)	Uniform elongation (%)	Total elongation (%)	Strength coefficient, K (MPa)
70	128	23.4	25.4	582
n-value	R_0	R_{45}	R_{90}	*Possion's Ratio* (ν)
0.33	0.75	0.85	0.85	0.33

2.3.2. Pre-straining, Annealing and Tensile Tests

To characterize the post-annealing material plastic properties, the material was subjected to various pre-straining and annealing conditions and tested in uniaxial tension on an Instron tensile machine, where load and strain data were recorded by the DIC system.

Pre-straining and Annealing

The large test specimens were pre-strained along the transverse direction in uniaxial tension, near-plane strain, and equibiaxial tension to 0.15 and 0.20 equivalent plastic strain for the uniaxial specimens, and to 0.20 equivalent plastic strain for the other two paths. The details on pre-strain specimen geometries, equipment, and forming parameters were introduced in Li et al. [2012]. The pre-strain of the uniaxial specimens was controlled via percent elongation using an extensometer with the Instron Bluehill software. However, the DIC system was used to check the pre-strain levels of near-plane strain and equibiaxial specimens by taking a before and after image of the deformed sheet, created in turn by the WF250 servo hydraulic press developed by Interlaken Technologies Corporation (ITC). This die set had a flat-bottom punch with diameter of 305 mm and lock beads in the blank holder with 400 mm diameter.

To achieve near-plane strain, panels cut to 304.8 mm by 431.8 mm (with the long side perpendicular to the rolling direction, RD) were stamped with a plastic lubricant and a steel carrier blank, with 200 mm center hole, using a clamp depth of -4.9 mm, a punch depth of 26 mm, and a peak blank holding force of 120 kN. To achieve equibiaxial strain, panels cut to 430 mm by 430 mm were stamped with a steel carrier blank, using a clamp depth of -4 mm, a punch depth of 22.1 mm, and a peak blank holding force of 600 kN. Note that the blank holding forces were experimentally chosen to prevent flow from material outside the lock beads.

Extracted from these sheets were two duplicate ASTM E8-08 tensile specimens of each orientation (15 degree increments from 0 to 90 degrees with respect to the RD). The gage section of each tensile bar was located in the center area of each of the large preform panels to ensure a nearly pure and uniform plane or biaxial pre-strain condition. They were then either not annealed (serving as a control group), or annealed in a salt bath at 350 °C for 10-second and 20-minute durations. Further experimental details associated with pre-straining and annealing can be found in Li et al. [2011].

<u>Conducting Uniaxial Tension Tests and Strain Measurement via DIC</u>

Since DIC was used to capture strain information, each specimen was cleaned and then lightly coated with a white spray paint. Following a short drying period, small black spray paint droplets (ranging from 0.5-1 mm) were applied. This enabled calculation of the grid points with the DIC software. Care was taken to ensure that no single black droplet exceeded the area of a pixel subset (29 pixels by 29 pixels) and that tests were performed the same day as paint application to avoid desiccation.

Stereo DIC is a non-contact optical method for measuring three-dimensional displacements and strain fields on a deforming surface [Reedlunn et al., 2011]. In the current research, the DIC system included image acquisition software Vic-Snap and post-processing package VIC-3D 2009 from Correlated Solutions, Inc. The DIC method compares digital images at a fixed framing rate to obtain a quantitative, point-by-point mapping of the deformation fields. The deformation strain is computed by optimizing a cross-correlation function to match the local gray scale intensity values of a reference image and a subsequent image of the deformed specimen surface. A sequence of images is captured by two cameras angled from 20 to 40 degrees with respect to the vertical, to obtain the deformation history during uniaxial tensile testing. In the current research, this is done with the image acquisition software, Vic-Snap. The reference image, taken as the first image of the undeformed specimen, is used to calculate the accumulated strain by comparing it with subsequent images of deformed material.

During post-processing, the Vic-3D software is used to decompose each image into a set of overlapping pixel subsets. The image correlation algorithm tracks the location of each subset from image-to-image and computes a grid point at the center of each subset, which is subsequently used to compute displacement and strain fields [Zavattieri et al., 2009]. In this way, the algorithm computes the displacement and strain fields of the deformed specimen. Strain accuracy of the system is up to 0.005%.

The tensile tests were conducted at a constant strain rate of 5 mm/min at ambient conditions using a 30 kN load cell. To automatically synchronize load data with the strain image time stamps, load data was collected using the analog input in the DIC system instead of the Bluehill software. The strain and strain rate data were then calculated from the stereo images via Vic 3D's post-processing functions. Load data was collected directly from the Instron machine.

2.3.3. Analysis of Stress

The true stress of the specimen in uniaxial tension was calculated based on load data recorded at each DIC image; the instantaneous cross-sectional area of the specimen can then be calculated using the following formula:

$$\sigma_{\mathrm{yy}} = \frac{P_{yy}}{A_{yy}} \tag{2.6}$$

where y defines the tensile direction; P_{yy} is the experimentally measured tensile load; and A_{yy} is the instantaneous cross-sectional area of the specimen, which can be expressed as:

$$A_{yy} = A_0 e^{-\varepsilon_{\mathrm{yy}} + (1-2\upsilon)\sigma_{\mathrm{yy}}\left(\frac{1}{E}\right)} \tag{2.7}$$

where $\varepsilon_{\mathrm{yy}}$ is the longitudinal strain, E is Young's Modulus, and υ is Poisson's ratio (the material properties for AA-5182-O are listed in Table 2.1). Note that A_{yy} is itself dependent on σ_{yy}. This is due to the fact that the current stress state affects the elastic strains, on which the total width and thickness strains are dependent. Consequently, the stress-state at the previous time step (or DIC image) was used to determine the cross-sectional area at the current time step, a reasonable approximation given the high data sampling rate.

The cross-sectional area, needed to calculate the true stress, varies at different points along the specimen. This is especially true in the neck upon its formation. Hence, the strain data was extracted solely in a small circular region from the localized neck, with a radius approximately equal to the thickness of the specimen [Bridgman, 1952]. Thus, the transverse strain in this region reflected the local width reduction due to necking. The small area of data extraction, with radius equal to the thickness of the sample, also ensured a uniaxial state of stress in that small region. The small circular region was also centered on the point of maximum strain on the image before first data loss, determined by visually inspecting the DIC images.

Furthermore, to maximize the strain level available to the DIC algorithm, all the images collected by the cameras were processed. The collection rate was 30 frames per second. For the as-received material, strains up to 0.48 were observed. However, data was typically fit for strains of no more than 0.30 for all specimens.

2.3.4. Modeling Procedure

As the strain hardening models only apply to the region corresponding to plastic deformation, it was necessary to determine the yield point of the material to begin the fitting process. This was done algorithmically by excluding data points from high strain to low strain in the stress-strain data set until the remaining points had a linear correlation of greater than 0.95 and then selecting the data point after that as the onset of yield. In doing so, the elastic region, characterized by Hooke's law (linear force-displacement relationship), was excluded from analysis.

It is necessary to remove load data after ultimate tensile strength (UTS) from the fitting region. Thus, all data after this point were also excluded, leaving the region from yield until UTS as the data subset for the empirical fitting.

2.3.5. Determination of Necking

As a material is deformed in tension, random heterogeneities in the material will result in some areas in which the reduction in cross-sectional area overcomes the material's strain hardening. In other words, the load will reach a maximum and the material will develop a neck, or local reduction in width more severe than the rest of the material. From this observation, a condition for the onset of necking can be derived – it is known as Considère's criterion [Considère, 1885]:

$$\left.\frac{d\sigma}{d\varepsilon}\right|_{\varepsilon=\varepsilon_n} = \sigma(\varepsilon_n) \tag{2.8}$$

The meaning of this equation is that the slope of the stress-strain curve during plastic deformation will intersect the stress-strain curve itself at the formation of the neck. This condition is helpful for judging the predictive power of a strain-hardening model. For instance, identification of the neck allowed a partitioned-analysis of the Pearson coefficient, or R^2 value of the candidate models, and conversely, the failure to identify a reasonable necking strain indicated a poor fit. Furthermore, identification of the neck was necessary to the modeling procedure of the Voce-Tangent model.

In particular, constructing the Voce-Tangent Model for a given stress-strain data set is a four-step process. First, the pure Voce law is fit to the data set corresponding to plastic deformation. Second, the intersection point of the slope of the empirically fit Voce law with the Voce law itself must be determined – this

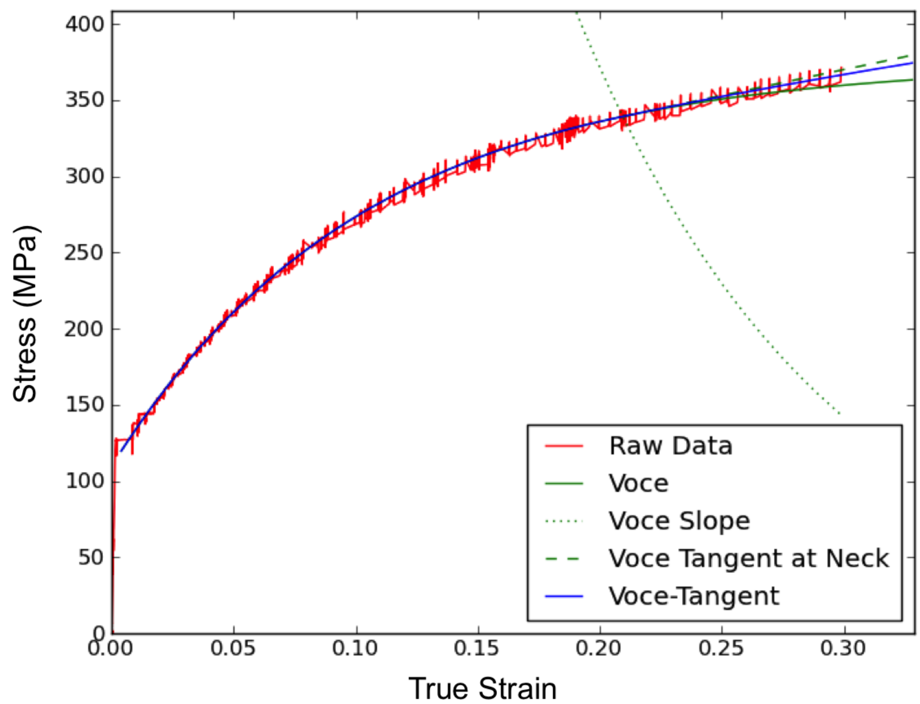

Fig 2.1 Visualization of constructing the Voce-Tangent model: the pure Voce law is first fit to the raw data, followed by a calculation of the necking point using the intersection of the slope of the Voce law and the Voce law itself. Then, the tangent at this point is constructed. The Voce-Tangent model is then a weighted mixture of the lower bound of the Voce law and the upper bound of its tangent.

identifies the onset of necking. Third, the tangent to the Voce law at necking is constructed at this point. Fourth, a weighting parameter that mixes the tangent and the Voce law is empirically determined; this bounds the data as the tangent tends to overshoot overestimate the true stress-strain values, serving as an upper bound to the Voce law's lower bound. This procedure is illustrated in Figure 2.1.

2.4 RESULTS AND DISCUSSION

Among the four candidate empirical models tested, the Voce-Tangent model performed the best in the post neck region for the as-received material. The Voce-Linear model, however, also performed well but was worse than the Voce-Tangent model overall.

2.4.1. As-received Material

The stress-strain models were compared for the as-received material in the 0-degree orientation (viz. AR-0), also known as the rolling direction (RD) of the sheet. As summarized in Figure 2.2, the Voce, Hollomon, Hollomon-Voce, Voce-Linear and Voce Tangent models are compared; Figure 2.2b is an enlargement of the post neck region. The models agree with the data well for most of the strain history (especially before necking), but they begin to diverge at higher strains. This is especially true for the Hollomon model, which shows noticeable deviation toward the end of the tensile test. The Hollomon model over-predicts the actual stresses while the Voce model under-predicts the stress slightly, indicating their possible use in forming upper and lower boundaries of a more accurate empirical fitting. Thus, the “mixed” models – the Hollomon-Voce and the Voce-Tangent models – each correct the pure Voce model’s deviation at high-strains. The Voce-Linear model similarly corrects the Voce

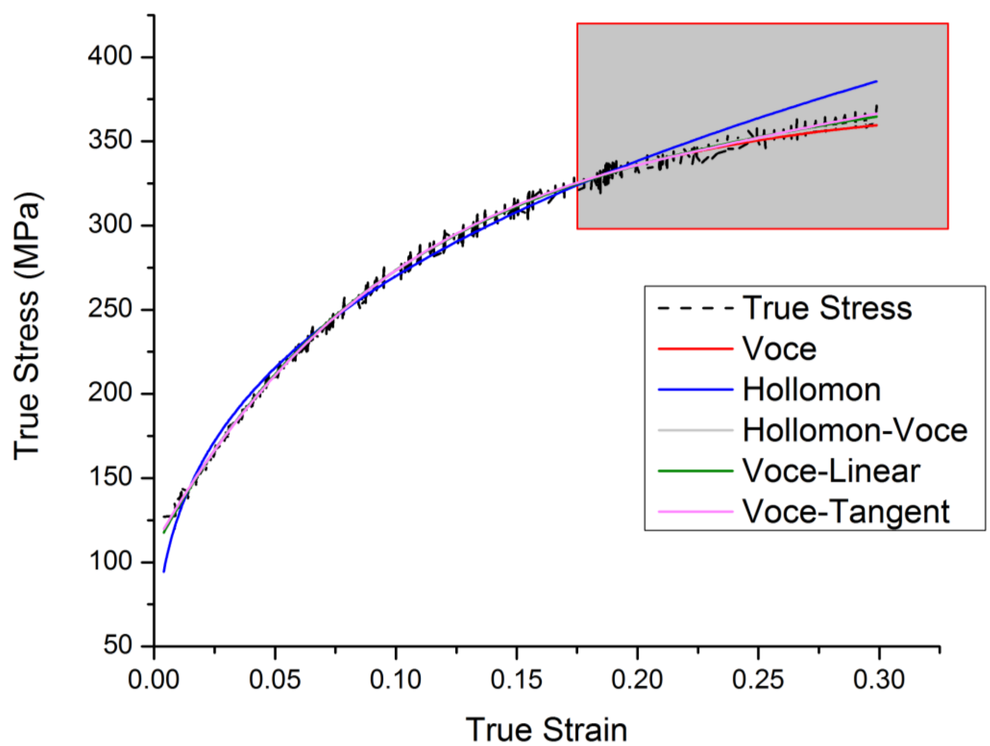

(a)

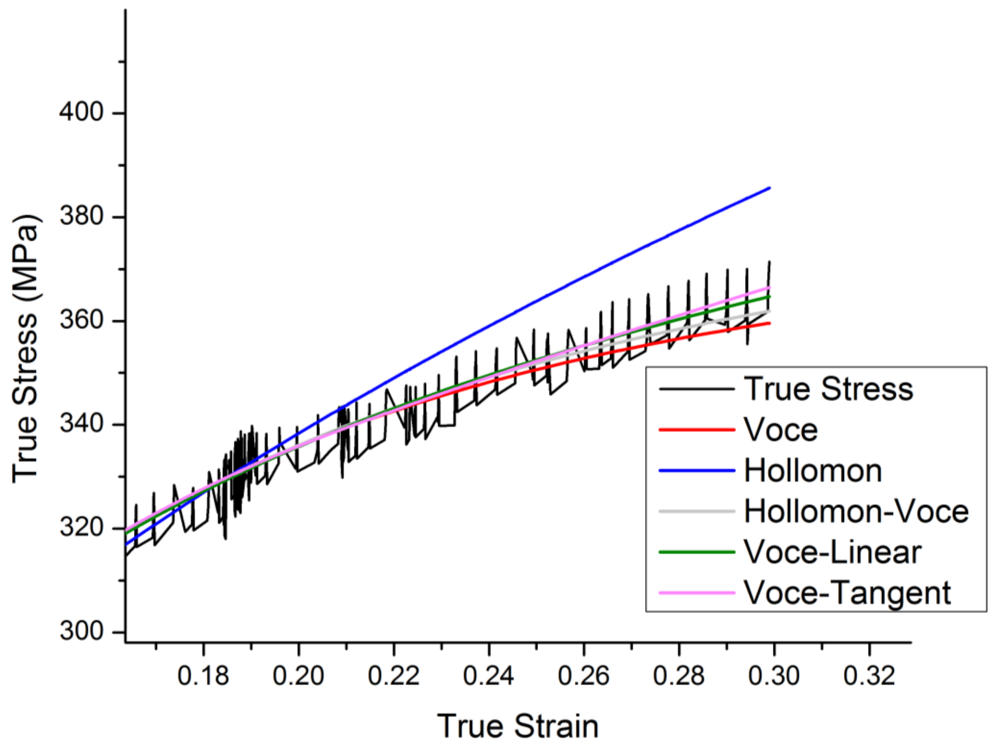

(b)

Figure 2.2 Comparison of strain hardening laws for different models (as-received AA-5182-O, 0 degree orientation): (a) true stress- true strain data with fitted curves, and (b) focus on the post-neck region (grey box in (a))

model, but does so by introducing a linear term during the entire strain history. Among these three models, the Hollomon-Voce model has the worst agreement with the data, which can be seen clearly from Figure 2.2b. The predictions from the Voce-Linear and the Voce-Tangent models are very close even in the post-neck region. Consequently, statistical parameters need to be examined to distinguish between them.

The statistical correlation parameter, R^2, indicates how well a function fits a set of data. This parameter essentially compares the variance of the difference between data points and the fitting function with the variance inherent in the data. As a result, this is a useful parameter for determining the predictive value of empirical fitting functions. The R^2 values for each model are tabulated in Table 2.2. It was generally not possible to tell a difference between the qualities of the empirical fittings within the first two decimal places. This is because the area of the divergence from the model and the data occurred after the onset of necking, an area in which there was less data. Thus, the R^2 values that were calculated for only the post-neck region were also considered as a basis of comparison. Table 2.2 shows that the Voce-Tangent model provided the best fit in the post-neck region, with an R^2 value of 0.83211, ~5-10% higher than the R^2 values of the other three models. It is noted that the Hollomon model cannot generally predict a reasonable necking point to determine the post-neck region, and thus no R^2 values were generated for this data subset.

Table 2.2 Comparison of the R^2 values for Voce, Hollomon, Hollomon-Voce, Voce-Linear and Voce-Tangent models for AR-0

	R^2_{Voce}	$R^2_{Hollomon}$	$R^2_{Hollomon-Voce}$	$R^2_{Voce-Linear}$	$R^2_{Voce-Tangent}$
The overall region	0.996841	0.991400	0.996883	0.997005	0.997016
The post-neck region	0.707337	Not Fit	0.735641	0.773586	0.83211(Best)

More R^2 values for the as-received specimens in other orientations are summarized in the Appendix. For the as-received AA5182-O, the Voce-Tangent model performed uniformly better than the other models, including the Voce-Linear model, despite their visual similarity. Even though the R^2 values in the post-neck region varied in quality, the Voce-Tangent appears to be superior to the Voce-Linear model in each case in the necking region. This is an expected result, as the Voce-Tangent model does not introduce a linear term into the fit until the onset of necking. Unlike the Voce-Linear model, where the linear term takes into account data during the entire tensile test, the Voce-Tangent model only corrects the Voce model after necking has occurred, increasing the tightness of the upper bound defined by the tangent.

Nevertheless, the Voce-Linear model was the closest competitor to the Voce-Tangent model. Due to its simple formulation and good performance compared to the Voce-Hollomon and Hollomon models, it will be explicitly discussed alongside the Voce-Tangent model in the subsequent sections regarding the effect of pre-strain and annealing. Data regarding the other models can be found in the appendix.

2.4.2. Orientation Effect on Strain Hardening

The fitted tensile true stress-strain curves of the as-received AA5182-O (by Voce-Tangent fitting) are compared in Figure 2.3 for orientations with 15-degree increments from 0 to 90 degrees with respect to the RD. The fitting parameters of the Voce or Voce-Tangent models are summarized in Table 2.3. It is observed that the strength of the RD (i.e. 0 degree) specimen is higher than the specimens in other orientations; and the strengths of the specimens in 30, 45, 60 and 75 degrees appear lower than others. This is reflected by the C parameter, which indicates how fast the material strain hardened. Therefore, a higher stress-strain curve indicates a higher absolute value of C; in this case, the specimen oriented in the 0 degree displayed the greatest degree of strain hardening. The trend of the C parameter along different orientations is summarized in Figure 2.4, where C has a maximum absolute value at 0 degrees, but lower absolute values at orientations of 30, 45, 60 and 75 degrees. The B parameter is the saturation stress and $A+B$ is the yield stress. There is no notable difference for these values across different orientations. As discussed in greater detail later, this appears to be directly linked with the crystallographic texture. The R^2 values of the Voce-Tangent (viz. VT) fitting for the regions before and after necking are 0.997 and 0.7-0.8 respectively.

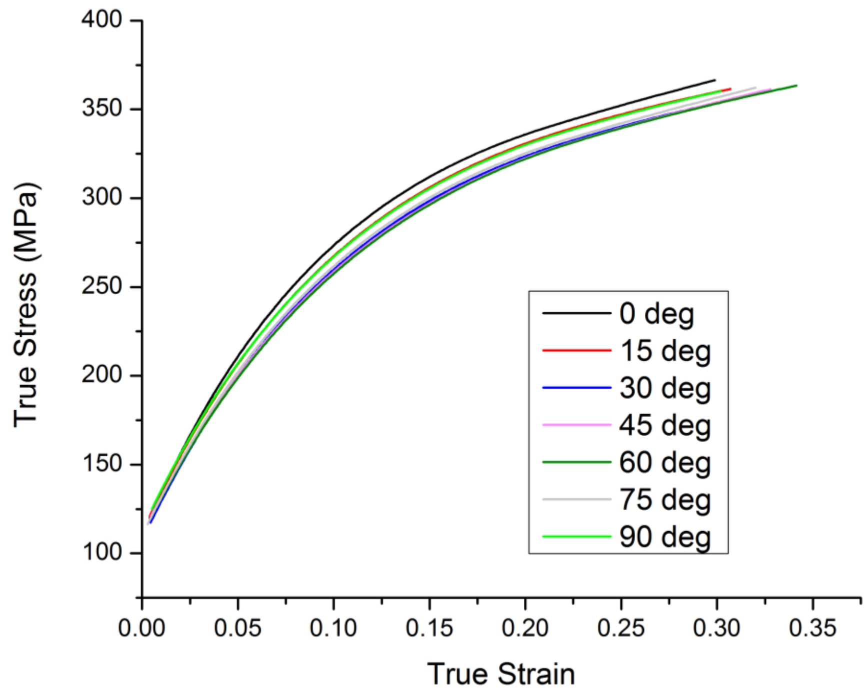

Figure 2.3 The fitted true stress- true strain curves of the as-received specimens in different orientations (by Voce-Tangent fitting)

Table 2.3 Voce parameters used in Voce and Voce-Tangent for as-received AA5182-O in different orientations

Angle from RD (deg)	0	15	30	45	60	75	90
A	374.001	372.885	369.651	371.953	374.126	370.887	373.771
B	-264.577	-261.932	-262.158	-260.645	-263.213	-261.015	-260.444
C	-9.609	-9.123	-8.698	-8.316	-8.233	-8.726	-8.917
A+B	109.424	110.953	107.493	111.308	110.913	109.871	113.327
R^2-VT	0.997	0.997	0.997	0.997	0.991	0.997	0.997
R^2 -VT-pn	0.832	0.789	0.828	0.823	0.496	0.773	0.718

2.4.3. Pre-strain Effect on the Stress-Strain Hardening

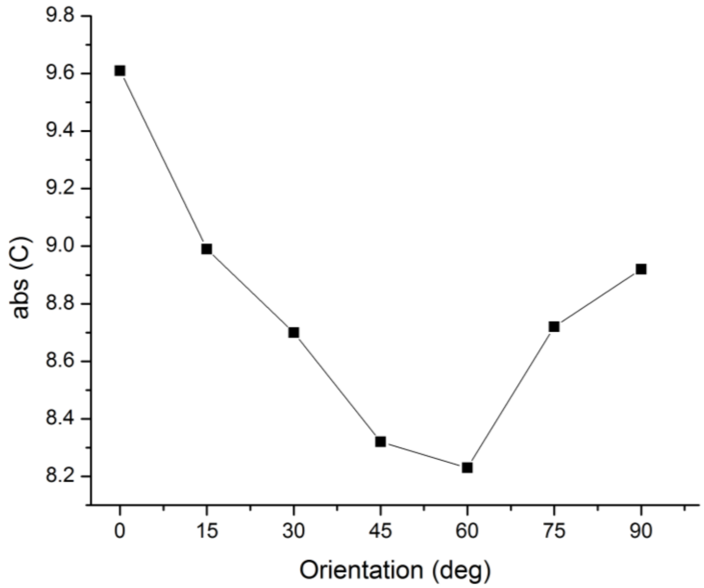

Figure 2.4 The Voce *C* parameter of the as-received specimens in different orientations

Li et al. [2013] proposed a constant initial ''effective plastic strain'' (EPS) to account for the effects of a given pre-strain. In that publication, only uniaxial pre-strain data were available. In the current research, the true stress- true strain curves of the equibiaxial (viz. EB) and plane strain (viz. PS) pre-strained specimens are compared to as-received specimen (viz. AR), as shown in Figure 2.5, where the pre-strain level was 0.2 with no subsequent annealing treatment. By overlapping the stress-strain curves for a best match of the plastic deformation region, the EPS is taken as the magnitude of the strain shift. For the 0.2 pre-strain no annealing condition, the EPS is 0.18 for both EB and PS pre-strained AA5182-O, which agrees with Li's results on uniaxial (viz. UA) pre-strained specimen. The 0.18 EPS is less than the pre-strain level (0.2) because of the stress relaxation due to unloading after pre-straining.

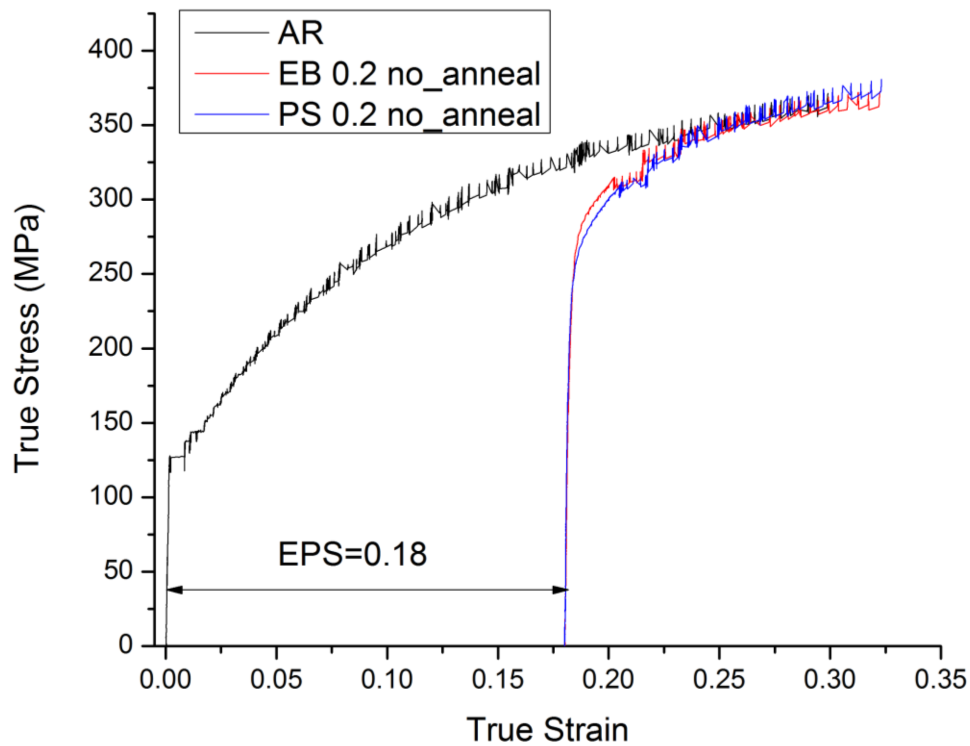

Figure 2.5 EPS method in accounting for pre-strain

The influence of pre-strain on the Voce parameters (from which the Voce-Tangent model is constructed) for different orientations (with 15-degree increments from 0 to 90 degrees with respect to the RD) are summarized in Figures 2.6 - 2.7 and the parameter data are listed in Appendix 2.A, where the pre-strained no anneal specimens (EB 0.2, PS 0.2 and UA 0.15) are compared with the AR specimens. EB pre-strained specimens show large variations and were excluded for |C| comparison. It is observed that pre-strain decreases *B* (saturation stress), and hence increases *A*+*B* (initial yield stress) as well as the absolute value of the *C* parameter. Additional pre-straining introduces greater change in the parameters. Changing orientation does not cause obvious variation in *B* or *A*+*B*; it does, however, decrease the *C* values when the pre-strained tensile specimens are oriented closer to 75 degrees, which is different than the trend in AR specimens. The R^2 values with Voce-Tangent (VT) fitting for the pre-strained specimen after necking region are around 0.4-0.7, which is lower than the AR material fittings. This suggests that the Voce-Tangent model may not predict the stresses accurately after the onset of necking for the cold worked materials.

However, despite the generally worse fitting in the post-necking region, the Voce-Tangent model was still able to generate a reasonable prediction of the necking point, thus making a calculation of the R^2 statistic in the post-neck area possible. This can be seen from Table 2.4, where despite the worse performance of the VT model compared to its own performance for the as-received material, the Voce-Linear model could not predict a reasonable necking point and thus no post-neck R^2 could be reported.

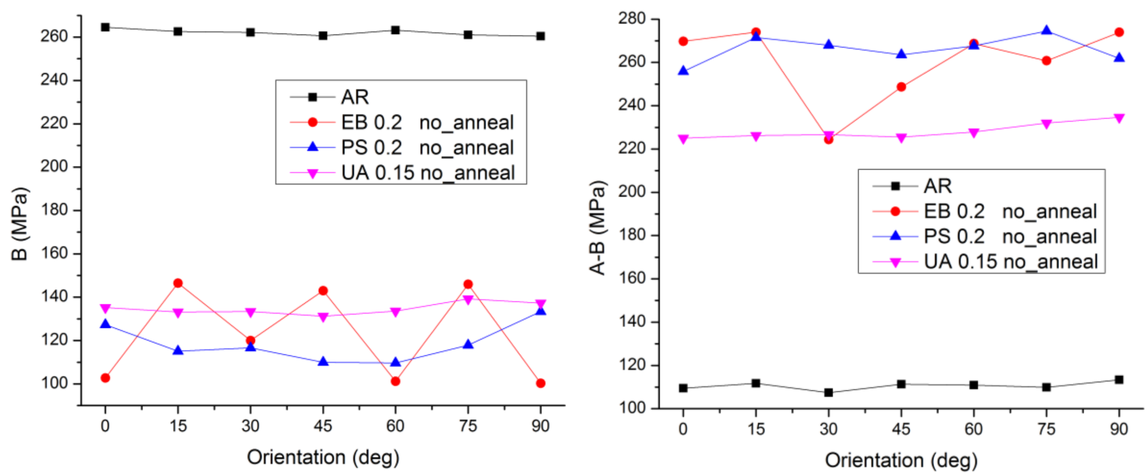

(a) (b)

Figure 2.6 Pre-strain effect on Voce parameters: (a) saturation stress, *B*; and (b) initial yield stress, *A* – *B*

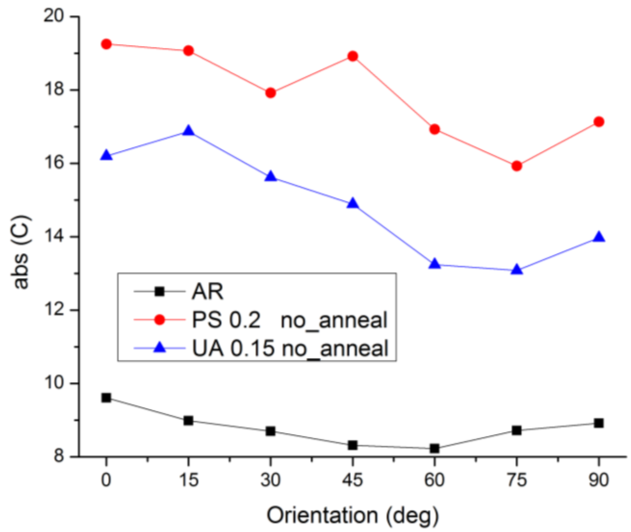

Figure 2.7 Pre-strain effect on Voce parameter *C*

Table 2.4 Comparison of the R^2 of the VT and VL models in the post-neck region for samples pre-strained in equibiaxial tension to 0.20 with no anneal

Angle from RD (deg)	0	15	30	45	60	75	90
R^2(VL-pn)	0.298	N/A	N/A	N/A	0.339	N/A	0.613
R^2(VT-pn)	0.549	0.273	0.568	0.533	0.302	0.574	0.615

2.4.4. Annealing Effect on Strain Hardening

The effect of annealing on strain hardening parameters is to reduce the effects of prior cold work in the material. This is equivalent to reducing the EPS shift caused by pre-strain, where the amount of reduction increases with annealing time, as illustrated in Figure 2.5.

Importantly, the performance of the Voce-Tangent model, as well as other models, improves as the annealing time increases. This is an expected result because the stored cold work in the material is either released through recovery (due to a short heat treatment, corresponding to the 10-second anneal) or transformed into new crystal grains through recrystallization (due to a long heat treatment, corresponding to the 20-minute anneal). Thus as the cold worked material is annealed, the material relieves internal stresses and becomes softer through recovery, recrystallization or grain growth rendering its mechanical properties close to its as-received state. Just as the Voce-Tangent model was superior at modeling the stress-strain response of the as-received material, the pre-strained material followed by anneal generally was characterized better by the Voce-Tangent model as well. However, this distinction was not as clear as it was for the as-received data.

Table 2.5 Comparison of the R^2 of the VT and VL models in the post-neck region for samples pre-strained in equibiaxial tension to 0.20 with 10-second anneal

Angle from RD (deg)	0	15	30	45	60	75	90
R^2(VL-pn)	N/A	0.686	0.763	0.63	0.607	0.666	0.674
R^2(VT-pn)	0.689	0.731	0.803	0.468	0.744	0.701	0.757

For samples annealed only to 10 seconds, the agreement between all models tested was generally worse, an effect magnified when considering only the post-neck region. In Table 2.5, for example, it can be seen that in general, the R^2 values in the post-neck region for the Voce-Tangent model is lower for the majority of orientations (15, 30, 45, 60, and 90 degree orientations). However, for the 20-minute anneal, the post-neck R^2 values are comparable to the as-received material.

On the other hand, the Voce-Linear model, often failed to fit the post-neck region of samples pre-strained and then annealed, despite the softening of the material. As reported in Table 2.6 for instance, the R^2 values in the post neck region could not be computed for the 30, 45, 60 and 75 degree orientations because the Voce-Linear model did not predict a reasonable necking point for those samples (as given by Considère's criterion [Considère, 1885]); in other words, the slope of the stress-strain curve only intersected the stress-strain curve itself after the sample had already fractured or was near fracture. A similar trend was observed with the Voce-Linear model for the specimens pre-strained in plane strain and equibiaxial tension to 0.20 and annealed for 20 minutes, although to a lesser extent.

Table 2.6 Comparison of the R^2 of the VT and VL models in the post-neck region for samples pre-strained in equibiaxial (EB), Plane strain (PS) and Uniaxial (UA) tension to 0.20 with 20-minute anneal

Angle from RD (deg)		0	15	30	45	60	75	90
EB	R^2(VL-pn)	0.775	0.772	0.785	0.83	0.817	N/A	0.859
	R^2(VT-pn)	0.644	0.802	0.809	0.814	0.901	0.409	0.905
PS	R^2(VL-pn)	0.924	0.67	0.756	0.792	0.746	N/A	N/A
	R^2(VT-pn)	0.953	0.73	0.789	0.83	0.758	0.701	0.737
UA	R^2(VL-pn)	0.747	0.944	N/A	N/A	N/A	N/A	0.742
	R^2(VT-pn)	0.775	0.961	0.705	0.911	0.891	0.848	0.865

Like the Voce-Tangent model, the R^2 values in the post neck region improved with annealing time, as can be seen from Table 2.6, where the comparable R^2 values for the EB-20 specimens are higher for the sample annealed for 20 minutes than the one annealed for 10 seconds. Furthermore, even when the post-neck R^2 values could be computed for the Voce-Linear model, its R^2 values were overall lower than the Voce-Tangent model.

As can be seen in Table 2.6, there is variation in the performance of the empirical models across orientation. Thus, the post-neck R^2 values, averaged across different specimen orientations, were also summarized in Figure 2.8.

Thus, overall the Voce-Tangent model outperformed all other models considered, including the Voce-Linear model. Although sometimes this improvement was around 5%, more dramatic improvements were noticed for different pre-strain and annealing combinations; these details can be found in the Appendix.

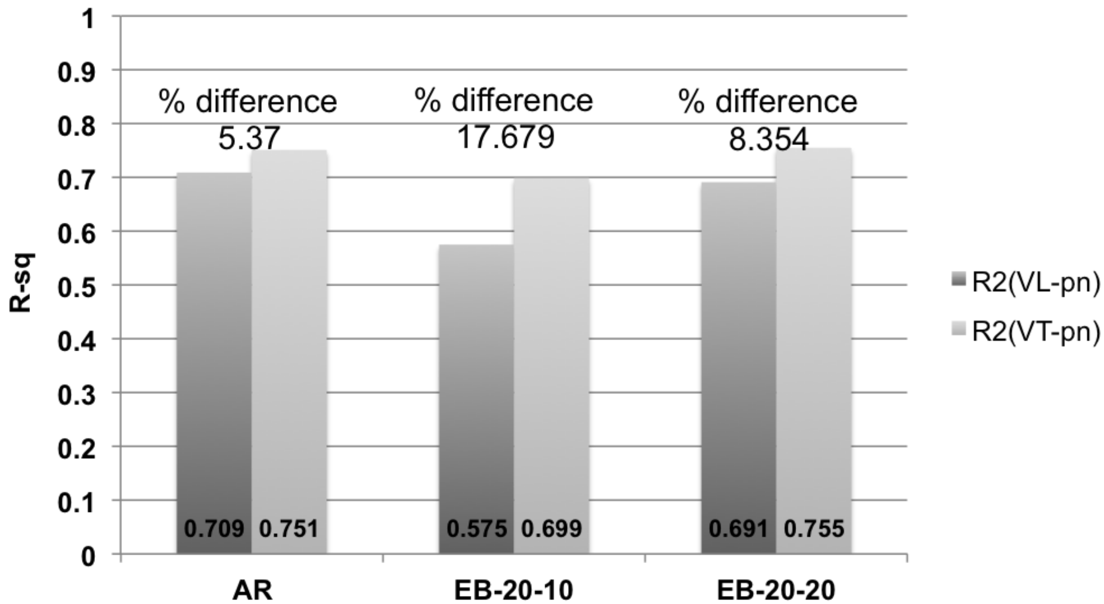

Figure 2.8 Comparisons of Average post-neck (pn) R^2 values for as-received (AR), Equibiaxial tension to 0.20 and annealed for 10 seconds at 350 °C (EB-20-10) and Equibiaxial tension to 0.20 and annealed for 20 minutes at 350 °C (EB-20-20) specimens

2.5 CONCLUSIONS

The strain hardening behavior of aluminum alloy 5182-O was discussed for different orientations, pre-strain and annealing conditions. The Voce-Tangent model was not only the most accurate model across all tested conditions in the critical post-neck region, but also the most robust method for fitting data at high strain.

1. It was validated that the EPS method (Li et al. 2013) is not only correct with uniaxial pre-strain but also with other pre-strain paths, e.g. plane strain and equibiaxial stretch.
2. The Voce parameter *C*, which- indicates how fast strain hardening is occurring, appears to be sensitive to orientation, whereas the *B* (saturation stress) and *A*+*B* (initial yield stress) parameters are not. Both pre-strain and annealing change the

strain hardening parameters as expected since such processes change the microstructure and mechanical behavior of most engineering materials.

3. The Voce-Tangent method is generally the most accurate model in the post-neck region, a key indicator of performance in large strain simulations. This is due to the fact that it only introduces an empirical mixing after necking has been identified. On average, this model performs 5 to 10% better than the other models in the post-neck region for the as-received material.
4. The accuracy of the Voce-Tangent model as well as the other models depends on the amount of cold work stored in the material. The greater this storage, the less accurate the models. However, the Voce-Tangent model was still observed to be the best fit even at the high pre-strain levels considered.
5. Annealing resets the cold work stored in a material, with the amount of resetting corresponding to the annealing condition (i.e. represented by time in this work). Thus, longer anneals made the material more amenable to empirical modeling in general; indeed, as the material became closer to its as-received state, the quality of the post-neck fit improved across all models, with the Voce-Tangent model again performing the best.

REFERENCES

Anand, L., (1982), “Constitutive equations for the rate-dependent deformation of metals at elevated temperatures,” Journal of Engineering Materials and Technology 104, 12–17.

Anand, L., (1985), “Constitutive equations for hot working of metals,” International Journal of Plasticity 1, 213–231.

Bodner, S.R., Partom, Y., (1975), “Constitutive equations for elastic–viscoplastic strain-hardening materials,” Journal of Applied Mechanics 46, 805–810.

Bridgman, P.W., (1952), Large Plastic Flow and Fracture. McGraw-Hill.

Brown, S.B., Kim, K.H., Anand, L., (1989), “An internal variable constitutive model for hot working of metals,” International Journal of Plasticity 5, 95–130.

Butuc, M.C., Gracio, J. J., Barata da Rocha, A., (2003), “A theoretical study on forming limit diagram prediction,” Journal of Materials Processing Technology, 142, 714-724.

Chen, S., Huang, C., Wang, C., Duan, Z., (2008), “Mechanical properties and constitutive relationships of 30CrMnSiA steel heated at high rate,” Materials Science and Engineering A, 105–108.

Considère, Armand, (1885), “Annales des Ponts et Chaussées,” 9, 574-775.

Follansbee, P.S., Kocks, U.F., (1988), “A constitutive description of the deformation of copper based on the use of the mechanical threshold stress as an internal state variable,” Acta Metallurgica 36, 81–93.

Hähner, P., (1996a), “On the Physics of the Portevin–Le Chatelier effect. Part 1: The statistics of dynamic strain ageing,” Materials Science and Engineering: A, 207, 208–215.

Hähner, P., (1996b), “On the Physics of the Portevin–Le Chatelier effect. Part 2: From microscopic to macroscopic behavior,” Materials Science and Engineering: A, 20, 216–223.

Hollomon, J. H., (1945), “Tensile deformation,” Transactions of the American Institute of Mining, Metallurgical and Petroleum Engineers, 162, 268- 290.

Jain, M., Lloyd, D. J., Macewen, S. R., (1996), “Hardening laws, surface roughness and biaxial tensile limit strains of sheet aluminum alloys,” The International Journal of Mechanical Sciences, 38, 219-232.

Johnson, G.R., Holmquist, T.J., (1988), “Evaluation of cylinder-impact test data for constitutive model constants,” Journal of Applied Mechanics, 64, 3901–3910.

Khan, A.S., Huang, S., (1992), “Experimental and theoretical study of mechanical behavior of 1100 aluminum in the strain rate range 10^{-5}–10^{4} s^{-1},” International Journal of

Plasticity 8, 397–424.

Khan, A.S., Liang, R., (1999), "Behaviors of three BCC metal over a wide range of strain rates and temperatures: experiments and modeling," International Journal of Plasticity 15, 1089–1109.

Khan, A.S., Suh, Y.S., Kazmi, R., (2004), "Quasi-static and dynamic loading responses and constitutive modeling of titanium alloys," International Journal of Plasticity 20, 2233–2248.

Kleemola, H.J., Nieminen, M.A., (1974), "On the strain-hardening parameters of metals," Metallurgical Transactions, 5, 1864.

Klepaczko, J.R., (1987), "A practical stress–strain-strain rate–temperature constitutive relation of the power form," Journal of Mechanical Working Technology, 15, 143–165.

Kocks, U.F., (1976), "Laws for work-hardening and low-temperature creep," ASME Journal of Engineering Materials and Technology, 98, 76–85.

Krajewski, P. E., (2007), "Method for production of stamped sheet metal panels," US Patent 7,260,972, B2.

Li, J., Hu, S. J., Carsley, J. E., Lee, T. M., Hector, Jr., L. G., Mishra, S., (2011), "Postanneal mechanical properties of pre-strained AA5182-O sheets," ASME Journal of Manufacturing Science and Engineering, 133, 061007-1-10.

Lin, M.R., Wagoner, R.H., (1987), "An experimental investigation of deformation induced heating during tensile testing," Metallurgical and Materials Transactions A, 18A, 1035–1042.

Ling, Y., (1996), "Uniaxial true stress-strain after necking" AMP Journal of Technology, 5, 37-48.

Mecking, H., Kocks, U.F., (1981), "Kinetics of flow and strain-hardening," Acta Metallurgica, 29, 1865–1875.

Reedlunn, B., Daly, S., Daly, Hector Jr., L., Zavattieri, P., Shaw, J., (2013), "Tips & tricks for characterizing shape memory wire Part 5: Full-field Strain Measurement by Digital Image Correlation," Experimental Techniques, 37, 62-78.

Rusinek, A., Klepaczko, J.R., (2001), "Shear testing of a sheet steel at wide range of strain rates and a constitutive relation with strain-rate and temperature dependence of the flow stress", International Journal of Plasticity, 17, 87–115.

Rusinek, A., Zaera, R., Klepaczko, J.R., (2007), "Constitutive relations in 3-D for a wide range of strain rates and temperatures – application to mild steels," International Journal of Solids and Structures 44, 5611–5631.

Sing, W.M., Rao, K.P., (1997), "Role of strain-hardening laws in the prediction of forming limit curves," Journal of Materials Processing Technology, 63, 105-110.

Sung, J. H., Kim, J. H., Wagoner, R. H., (2010), "A plastic constitutive equation incorporating strain, strain-rate, and temperature," International Journal of Plasticity, 26, 1746-1771.

Swift, H.W., (1952), "Plastic instability under plane stress," Journal of the Mechanics and Physics of Solids, 1, 1-18.

Tome, C., Canova, G.R., Kocks, U.F., Christodoulous, N., Jonas, J.J., (1984), "The relation between macroscopic and microscopic strain hardening in F.C.C. polycrystals," Acta Metallurgica, 32, 1637-1653.

Voce, E., (1955), A practical strain hardening function. Metallurgia, 51, 219–226.

Zavattieri, P. D., Savic, V., Hector Jr., L.G., Fekete, J. R., Tong, W. Xuan, Y., 2009, "Spatio-temporal characteristics of the Portevin-Le Chatelier effect in austenitic steel with twinning induced plasticity," International Journal of Plasticity, 25, 2298-2330.

Zerilli, F.J., Ronald, R.W., (1987), "Description of tantalum deformation behavior by dislocation mechanics based constitutive relations," Journal of Applied Mechanics, 68, 1580–1591.

Appendix 2.A As-received (AR) Data and Parameters

Appendix 2.A.1 R^2 values for as-received material at different orientations and different empirical fits: Voce (V), Hollomon (H), Hollomon-Voce (VH), Voce-Line (VL), Voce-Tangent (VT).

Angle from RD (deg)	0	15	30	45	60	75	90
R^2(V)	0.997	0.997	0.997	0.997	0.991	0.997	0.997
R^2(H)	0.991	0.991	0.991	0.992	0.985	0.992	0.992
R^2(VH)	0.997	0.997	0.997	0.997	0.991	0.997	0.997
R^2(VL)	0.997	0.997	0.997	0.997	0.991	0.997	0.997
R^2(VT)	0.997	0.997	0.997	0.997	0.991	0.997	0.997

Appendix 2.A.2 R2 values in only the post-neck region (pn) for as-received material at different orientations and different empirical fits: Voce (V), Hollomon (H), Hollomon-Voce (VH), Voce-Line (VL), Voce-Tangent (VT).

Angle from RD (deg)	0	15	30	45	60	75	90
R^2(V-pn)	0.707	0.723	0.778	0.733	0.453	0.65	0.684
R^2(H-pn)	N/A	N/A	N/A	N/A	N/A	N/A	N/A
R^2(VH-pn)	0.736	0.721	0.763	0.768	0.466	0.724	0.701
R^2(VL-pn)	0.774	0.73	0.763	0.783	0.47	0.734	0.709
R^2(VT-pn)	0.832	0.789	0.828	0.823	0.496	0.773	0.718

Appendix 2.A.3 Average post-neck (pn) R^2 values for as-received material and percent difference with respect to the maximum R^2 value.

	Average	% difference
R^2(V-pn)	0.676	10.063
R^2(H-pn)	N/A	N/A
R^2(VH-pn)	0.697	7.24
R^2(VL-pn)	0.709	5.637
R^2(VT-pn)	0.751	0

Appendix 2.A.4 As-received parameters used in Voce (V) model (Eqn. 2.1)

Angle from RD (deg)	0	15	30	45	60	75	90
A	374.001	372.885	369.651	371.953	374.126	370.887	373.771
B	-264.577	-261.932	-262.158	-260.645	-263.213	-261.015	-260.444
C	-9.609	-9.123	-8.698	-8.316	-8.233	-8.726	-8.917

Appendix 2.A.5 As-received parameters used in Hollomon (H) model (Eqn. 2.2)

Angle from RD (deg)	0	15	30	45	60	75	90
K	569.072	557.452	548.008	540.637	541.957	545.327	553.344
N	0.325	0.323	0.328	0.323	0.324	0.322	0.32

Appendix 2.A.6 As-received additional parameters used in Voce-Hollomon (VH) model (Eqn. 2.3)

Angle from RD (deg)	0	15	30	45	60	75	90
α	0.924	0.939	0.903	0.891	0.892	0.876	0.934

Appendix 2.A.8 As-received parameters used in Voce-Linear (VL) model (Eqn. 2.4)

Angle from RD (deg)	0	15	30	45	60	75	90
A'	332.329	337.359	327.695	323.198	327.617	317.813	339.098
B'	-225.489	-228.094	-222.323	-214.626	-219.5	-210.89	-227.587
C'	-11.356	-10.445	-10.253	-10.15	-9.955	-10.865	-10.2
D'	129.939	106.631	120.435	135.331	125.749	154.146	101.077

Appendix 2.A.7 As-received additional parameters used in Voce-Tangent (VT) model (Eqn. 2.5)

Angle from RD (deg)	0	15	30	45	60	75	90
ε_n	0.21	0.215	0.222	0.226	0.227	0.22	0.217
w	0.332	0.471	0.517	0.419	0.601	0.341	0.523

Appendix 2.B Material Pre-strained in Equibiaxial tension to 0.20 without Anneal (EB-20-0) Data and Parameters

Appendix 2.B.1 R^2 values for material pre-strained in Equibiaxial (EB) tension to 0.20 without anneal at different orientations for different empirical fits: Voce (V), Hollomon (H), Hollomon-Voce (VH), Voce-Line (VL), Voce-Tangent (VT).

Angle from RD (deg)	0	15	30	45	60	75	90
R^2(V)	0.96	0.947	0.969	0.718	0.964	0.973	0.967
R^2(H)	0.967	0.951	N/A	0.721	0.959	0.973	0.967
R^2(VH)	0.967	0.952	0.969	0.721	0.964	0.974	0.969
R^2(VL)	0.961	0.966	0.991	N/A	0.965	0.976	0.968
R^2(VT)	0.96	0.948	0.977	0.718	0.964	0.973	0.968

Appendix 2.B.2 R^2 values in only the post-neck region (pn) for material pre-strained in Equibiaxial (EB) tension to 0.20 without anneal at different orientations for different empirical fits: Voce (V), Hollomon (H), Hollomon-Voce (VH), Voce-Line (VL), Voce-Tangent (VT).

Angle from RD (deg)	0	15	30	45	60	75	90
R^2(V-pn)	0.522	0.163	N/A	0.461	0.302	0.523	0.594
R^2(H-pn)	0.28	0.215	N/A	0.352	0.094	0.519	0.536
R^2(VH-pn)	0.353	N/A	0.969	0.391	0.321	0.553	0.596
R^2(VL-pn)	0.298	N/A	N/A	N/A	0.339	N/A	0.613
R^2(VT-pn)	0.549	0.273	0.568	0.533	0.302	0.574	0.615

Appendix 2.B.3 Average post-neck (pn) R^2 values for material pre-strained in Equibiaxial (EB) tension to 0.20 without anneal, as well as percent difference with respect to the maximum R^2 value.

	Average	% difference
R^2(V-pn)	0.366	24.892
R^2(H-pn)	0.285	41.487
R^2(VH-pn)	0.455	6.783
R^2(VL-pn)	0.179	63.351
R^2(VT-pn)	0.488	0

Appendix 2.B.4 Equibiaxial pre-strain to 0.20 without anneal parameters used in Voce (V) model (Eqn. 2.1)

Angle from RD (deg)	0	15	30	45	60	75	90
A	370.279	420.47	331.643	402.087	369.071	406.748	373.435
B	-103.823	-146.491	-325.855	-145.06	-101.489	-145.952	-100.594
C	-22.519	-6.213	-265.503	-9.143	-17.987	-8.396	-18.713

Appendix 2.B.5 Equibiaxial pre-strain to 0.20 without anneal parameters used in Hollomon (H) model (Eqn. 2.2)

Angle from RD (deg)	0	15	30	45	60	75	90
K	448.354	451.837	N/A	476.015	440.77	475.186	445.721
N	0.097	0.121	N/A	0.143	0.099	0.141	0.096

Appendix 2.B.6 Equibiaxial pre-strain to 0.20 without anneal additional parameters used in Voce-Hollomon (VH) model (Eqn. 2.3)

Angle from RD (deg)	0	15	30	45	60	75	90
α	0.123	0.328	1	0.085	0.975	0.481	0.546

Appendix 2.B.8 Equibiaxial pre-strain to 0.20 without anneal parameters used in Voce-Linear (VL) model (Eqn. 2.4)

Angle from RD (deg)	0	15	30	45	60	75	90
A'	331.009	295.648	291.73	145.383	434.992	296.463	346.326
B'	-70.542	-122.653	-298.21	-1436.21	-165.397	-85.821	-76.354
C'	-40.556	-74.753	-393.158	-71.813	-11.835	-48.579	-26.221
D'	289.365	448.317	685.754	246.84	-316.38	459.455	166.256

Appendix 2.B.7 Equibiaxial pre-strain to 0.20 without anneal additional parameters used in Voce-Tangent (VT) model (Eqn. 2.5)

Angle from RD (deg)	0	15	30	45	60	75	90
ε_n	0.084	0.148	0.021	0.142	0.092	0.145	0.089
w	0.78	0	0.091	0.13	1	0	0.752

Appendix 2.C Material Pre-strained in Plane Strain tension to 0.20 without Anneal (PS-20-0) Data and Parameters

Appendix 2.C.1 R^2 values for material pre-strained in Plane Strain (PS) to 0.20 without anneal at different orientations for different empirical fits: Voce (V), Hollomon (H), Hollomon-Voce (VH), Voce-Line (VL), Voce-Tangent (VT).

Angle from RD (deg)	0	15	30	45	60	75	90
R^2(V)	0.979	0.972	0.975	0.977	0.975	0.971	N/A
R^2(H)	0.981	0.972	0.973	0.98	0.972	0.955	N/A
R^2(VH)	0.982	0.974	0.976	0.981	0.976	0.971	N/A
R^2(VL)	0.98	0.973	0.975	0.979	0.975	N/A	N/A
R^2(VT)	0.552	0.612	0.529	0.539	0.621	0.254	N/A

Appendix 2.C.2 R^2 values in only the post-neck region (pn) for material pre-strained in Plane Strain (PS) tension to 0.20 without anneal at different orientations for different empirical fits: Voce (V), Hollomon (H), Hollomon-Voce (VH), Voce-Line (VL), Voce-Tangent (VT).

Angle from RD (deg)	0	15	30	45	60	75	90
R^2(V-pn)	0.512	0.599	0.52	0.502	0.607	0.254	N/A
R^2(H-pn)	N/A	0.223	0.318	0.342	0.601	0.09	N/A
R^2(VH-pn)	0.346	0.558	0.503	0.443	0.628	0.327	N/A
R^2(VL-pn)	N/A	0.597	0.531	0.454	0.634	N/A	N/A
R^2(VT-pn)	0.552	0.612	0.529	0.539	0.621	0.254	N/A

Appendix 2.C.3 Average post-neck (pn) R2 values for material pre-strained in Plane Strain (PS) tension to 0.20 without anneal, as well as percent difference with respect to the maximum R2 value.

	Average	% difference
R^2(V-pn)	0.428	3.616
R^2(H-pn)	0.225	49.341
R^2(VH-pn)	0.401	9.757
R^2(VL-pn)	0.317	28.676
R^2(VT-pn)	0.444	0

Appendix 2.C.4 Plane Strain pre-strain to 0.20 without anneal parameters used in Voce (V) model (Eqn. 2.1)

Angle from RD (deg)	0	15	30	45	60	75	90
A	381.768	385.409	383.457	372.699	376.758	392.357	199.288
B	-127.761	-115.532	-116.989	-110.554	-109.882	-117.851	-67.303
C	-19.965	-19.748	-18.503	-19.474	-17.22	-15.957	-7.944

Appendix 2.C.5 Plane Strain pre-strain to 0.20 without anneal parameters used in Hollomon (H) model (Eqn. 2.2)

Angle from RD (deg)	0	15	30	45	60	75	90
K	484.157	474.317	469.818	453.382	449.473	470.125	245.893
N	0.124	0.109	0.111	0.106	0.102	0.108	0.062

Appendix 2.C.6 Plane Strain pre-strain to 0.20 without anneal additional parameters used in Voce-Hollomon (VH) model (Eqn. 2.3)

Angle from RD (deg)	0	15	30	45	60	75	90
α	0.419	0.519	0.675	0.209	0.664	1	1

Appendix 2.C.8 Plane Strain pre-strain to 0.20 without anneal parameters used in Voce-Linear (VL) model (Eqn. 2.4)

Angle from RD (deg)	0	15	30	45	60	75	90
A'	345.051	364.976	372.591	329.367	353.724	227.171	193.023
B'	-96.145	-97.016	-106.842	-75.863	-88.736	-88.448	-61.499
C'	-32.143	-24.215	-20.337	-36.897	-22.036	-5.606	-8.757
D'	260.386	127.716	63.521	276.582	127.097	-139.993	30.674

Appendix 2.C.7 Plane Strain pre-strain to 0.20 without anneal additional parameters used in Voce-Tangent (VT) model (Eqn. 2.5)

Angle from RD (deg)	0	15	30	45	60	75	90
ε_n	0.098	0.093	0.096	0.093	0.097	0.102	0.055
w	0.533	0.8	0.807	0.751	0.826	1	0.825

Appendix 2.D Material Pre-strained in Unaxial tension to 0.15 without Anneal (UA-15-0) Data and Parameters

Appendix 2.D.1 R^2 values for material pre-strained in Uniaxial (UA) tension to 0.15 without anneal at different orientations for different empirical fits: Voce (V), Hollomon (H), Hollomon-Voce (VH), Voce-Line (VL), Voce-Tangent (VT).

Angle from RD (deg)	0	15	30	45	60	75	90
R^2(V)	0.985	0.984	0.985	0.985	0.985	0.985	0.987
R^2(H)	0.982	0.983	0.981	0.98	0.981	0.975	0.984
R^2(VH)	0.986	0.986	0.986	0.985	0.986	0.985	0.988
R^2(VL)	0.985	0.984	0.986	0.985	0.987	0.985	0.988
R^2(VT)	0.985	0.984	0.985	0.985	0.986	0.985	0.988

Appendix 2.D.2 R^2 values in only the post-neck region (pn) for material pre-strained in Uniaxial (UA) tension to 0.15 without anneal at different orientations for different empirical fits: Voce (V), Hollomon (H), Hollomon-Voce (VH), Voce-Line (VL), Voce-Tangent (VT).

Angle from RD (deg)	0	15	30	45	60	75	90
R^2(V-pn)	0.593	0.565	0.686	0.67	0.667	0.646	0.642
R^2(H-pn)	N/A	0.308	0.118	0.502	0.748	0.599	0.533
R^2(VH-pn)	0.594	0.606	0.703	0.698	0.725	0.679	0.658
R^2(VL-pn)	0.578	0.576	0.724	0.717	0.766	0.688	0.663
R^2(VT-pn)	0.636	0.613	0.726	0.709	0.758	0.665	0.693

Appendix 2.D.3 Average post-neck (pn) R2 values for material pre-strained in Unaxial (UA) tension to 0.15, as well as percent difference with respect to the maximum R2 value.

	average	% difference
R^2(V-pn)	0.638	6.903
R^2(H-pn)	0.401	41.531
R^2(VH-pn)	0.666	2.851
R^2(VL-pn)	0.673	1.82
R^2(VT-pn)	0.686	0

Appendix 2.D.4 Uniaxial pre-strain to 0.15 without anneal parameters used in Voce (V) model (Eqn. 2.1)

Angle from RD (deg)	0	15	30	45	60	75	90
A	359.627	358.072	359.452	356.241	361.083	371.156	371.968
B	-135.542	-133.592	-133.599	-131.382	-133.756	-139.292	-137.267
C	-16.491	-17.482	-15.835	-15.086	-13.395	-13.125	-13.974

Appendix 2.D.5 Uniaxial pre-strain to 0.15 without anneal parameters used in Hollomon (H) model (Eqn. 2.2)

Angle from RD (deg)	0	15	30	45	60	75	90
K	459.183	453.761	453.041	443.942	442.719	455.555	462.774
N	0.141	0.135	0.138	0.135	0.136	0.138	0.139

Appendix 2.D.6 Uniaxial pre-strain to 0.15 without anneal additional parameters used in Voce-Hollomon (VH) model (Eqn. 2.3)

Angle from RD (deg)	0	15	30	45	60	75	90
α	0.732	0.548	0.784	0.77	0.703	0.913	0.764

Appendix 2.D.7 Uniaxial pre-strain to 0.15 without anneal parameters used in Voce-Linear (VL) model (Eqn. 2.4)

Angle from RD (deg)	0	15	30	45	60	75	90
A'	348.716	321.087	335.54	327.088	317.575	362.044	333.245
B'	-126.446	-99.883	-111.965	-104.719	-94.716	-131.482	-102.156
C'	-20.111	-25.031	-19.544	-19.616	-20.588	-15.051	-19.793
D'	68.507	215.881	117.849	141.581	195.794	38.996	183.361

Appendix 2.D.8 Uniaxial pre-strain to 0.15 without anneal additional parameters used in Voce-Tangent (VT) model (Eqn. 2.5)

Angle from RD (deg)	0	15	30	45	60	75	90
ε_n	0.114	0.111	0.116	0.118	0.125	0.127	0.122
w	0.78	0.502	0.745	0.691	0.613	0.836	0.58

Appendix 2.E Material Pre-strained in Equibiaxial tension to 0.20 with 10 second anneal (EB-20-10) Data and Parameters

Appendix 2.E.1 R^2 values for material pre-strained in Equibiaxial (EB) tension to 0.20 and annealed for 10 seconds at 350 C, at different orientations for different empirical fits: Voce (V), Hollomon (H), Hollomon-Voce (VH), Voce-Line (VL), Voce-Tangent (VT).

Angle from RD (deg)	0	15	30	45	60	75	90
R^2(V)	0.951	0.994	0.994	0.987	0.994	0.994	0.995
R^2(H)	N/A	0.988	0.988	0.982	0.989	0.991	0.988
R^2(VH)	0.951	0.994	0.995	0.988	0.995	0.995	0.995
R^2(VL)	0.985	0.994	0.995	0.988	0.995	0.995	0.995
R^2(VT)	0.954	0.994	0.995	0.987	0.995	0.994	0.995

Appendix 2.E.2 R^2 values in only the post-neck region (pn) for material pre-strained in Equibiaxial (EB) tension to 0.20 and annealed for 10 seconds at 350 C, at different orientations for different empirical fits: Voce (V), Hollomon (H), Hollomon-Voce (VH), Voce-Line (VL), Voce-Tangent (VT).

Angle from RD (deg)	0	15	30	45	60	75	90
R^2(V-pn)	0.284	0.681	0.67	0.438	0.654	0.624	0.691
R^2(H-pn)	N/A	N/A	0.299	0.265	0.328	N/A	N/A
R^2(VH-pn)	0.285	0.695	0.712	0.446	0.681	0.683	0.695
R^2(VL-pn)	N/A	0.686	0.763	0.63	0.607	0.666	0.674
R^2(VT-pn)	0.689	0.731	0.803	0.468	0.744	0.701	0.757

Appendix 2.E.3 Average post-neck (pn) R^2 values for material pre-strained in Equibiaxial (EB) tension to 0.20 and annealed for 10 seconds at 350 C, as well as percent difference with respect to the maximum R^2 value.

	average	% difference
R^2(V-pn)	0.578	17.365
R^2(H-pn)	0.127	81.768
R^2(VH-pn)	0.6	14.209
R^2(VL-pn)	0.575	17.679
R^2(VT-pn)	0.699	0

Appendix 2.E.4 Equibiaxial pre-strain to 0.20 with 10 second anneal parameters used in Voce (V) model (Eqn. 2.1)

Angle from RD (deg)	0	15	30	45	60	75	90
A	358.105	405.437	375.84	376.377	375.52	373.683	377.966
B	-235.032	-241.916	-199.838	-201.215	-199.217	-198.059	-201.555
C	-22.867	-9.253	-11.071	-10.673	-10.911	-11.068	-11.267

Appendix 2.E.5 Equibiaxial pre-strain to 0.20 with 10 second anneal parameters used in Hollomon (H) model (Eqn. 2.2)

Angle from RD (deg)	0	15	30	45	60	75	90
K	254.83	552.551	500.795	499.626	499.423	500.541	507.904
N	0.104	0.262	0.212	0.214	0.212	0.214	0.214

Appendix 2.E.6 Equibiaxial pre-strain to 0.20 with 10 second anneal additional parameters used in Voce-Hollomon (VH) model (Eqn. 2.3)

Angle from RD (deg)	0	15	30	45	60	75	90
α	0.946	0.943	0.796	0.774	0.751	0.676	0.812

Appendix 2.E.7 Equibiaxial pre-strain to 0.20 with 10 second anneal parameters used in Voce-Linear (VL) model (Eqn. 2.4)

Angle from RD (deg)	0	15	30	45	60	75	90
A'	289.65	417.367	323.467	314.286	313.35	308.592	329.037
B'	-211.82	-253.938	-150.743	-143.439	-140.986	-138.352	-155.621
C'	-224.721	-10.163	-14.983	-15.535	-15.851	-16.793	-14.807
D'	453.234	12.451	195.734	229.212	237.071	248.964	186.213

Appendix 2.E.8 Equibiaxial pre-strain to 0.20 with 10 second anneal additional parameters used in Voce-Tangent (VT) model (Eqn. 2.5)

Angle from RD (deg)	0	15	30	45	60	75	90
ε_n	0.13	0.202	0.168	0.172	0.169	0.168	0.167
w	0.217	0.223	0.298	0.236	0.18	0.374	0.379

Appendix 2.F Material Pre-strained in Plane Strain to 0.20 with 10 second anneal (PS-20-10) Data and Parameters

Appendix 2.F.1 R^2 values for material pre-strained in Plane Strain (PS) to 0.20 and annealed for 10 seconds at 350 C, at different orientations for different empirical fits: Voce (V), Hollomon (H), Hollomon-Voce (VH), Voce-Line (VL), Voce-Tangent (VT).

Angle from RD (deg)	0	15	30	45	60	75	90
R^2(V)	N/A	0.983	0.995	0.984	0.994	0.914	N/A
R^2(H)	N/A	0.98	0.991	0.984	0.993	0.894	N/A
R^2(VH)	N/A	0.983	0.995	0.985	0.994	0.914	N/A
R^2(VL)	N/A	0.984	0.995	0.985	0.994	N/A	N/A
R^2(VT)	N/A	0.984	0.995	0.984	0.994	0.914	N/A

Appendix 2.F.2 R^2 values in only the post-neck region (pn) for material pre-strained in Plane Strain (PS) to 0.20 and annealed for 10 seconds at 350 C, at different orientations for different empirical fits: Voce (V), Hollomon (H), Hollomon-Voce (VH), Voce-Line (VL), Voce-Tangent (VT).

Angle from RD (deg)	0	15	30	45	60	75	90
R^2(V-pn)	N/A	0.701	0.75	0.609	0.694	0.691	N/A
R^2(H-pn)	N/A	0.546	N/A	0.553	0.951	N/A	N/A
R^2(VH-pn)	N/A	0.733	0.729	0.615	0.739	N/A	N/A
R^2(VL-pn)	N/A	0.802	0.709	-0.381	0.791	N/A	N/A
R^2(VT-pn)	N/A	0.867	0.788	0.782	0.854	0.691	N/A

Appendix 2.F.3 Average post-neck (pn) R^2 values for material pre-strained in Plane Strain (PS) tension to 0.20 and annealed for 10 seconds at 350 C, as well as percent difference with respect to the maximum R^2 value.

	average	% difference
R^2(V-pn)	0.689	13.491
R^2(H-pn)	0.41	48.51
R^2(VH-pn)	0.563	29.307
R^2(VL-pn)	0.46	42.198
R^2(VT-pn)	0.796	0

Appendix 2.F.4 Plane Strain pre-strain to 0.20 with 10 second anneal parameters used in Voce (V) model (Eqn. 2.1)

Angle from RD (deg)	0	15	30	45	60	75	90
A	N/A	409.959	385.997	405.244	414.743	720.505	N/A
B	N/A	-256.076	-214.106	-247.715	-265.341	-547.95	N/A
C	N/A	-8.536	-10.356	-7.314	-6.134	-2.254	N/A

Appendix 2.F.5 Plane Strain pre-strain to 0.20 with 10 second anneal parameters used in Hollomon (H) model (Eqn. 2.2)

Angle from RD (deg)	0	15	30	45	60	75	90
K	N/A	574.051	519.183	533.62	550.149	627.897	N/A
N	N/A	0.282	0.226	0.272	0.306	0.337	N/A

Appendix 2.F.6 Plane Strain pre-strain to 0.20 with 10 second anneal additional parameters used in Voce-Hollomon (VH) model (Eqn. 2.3)

Angle from RD (deg)	0	15	30	45	60	75	90
α	N/A	0.938	0.75	0.49	0.783	1	N/A

Appendix 2.F.7 Plane Strain pre-strain to 0.20 with 10 second anneal parameters used in Voce-Linear (VL) model (Eqn. 2.4)

Angle from RD (deg)	0	15	30	45	60	75	90
A'	N/A	350.891	331.305	282.734	331.899	N/A	N/A
B'	N/A	-201.268	-162.92	-135.391	-187.358	N/A	N/A
C'	N/A	-10.994	-13.877	-14.731	-8.552	N/A	N/A
D'	N/A	172.831	191.653	353.155	191.887	N/A	N/A

Appendix 2.F.8 Plane Strain pre-strain to 0.20 with 10 second anneal additional parameters used in Voce-Tangent (VT) model (Eqn. 2.5)

Angle from RD (deg)	0	15	30	45	60	75	90
ε_n	N/A	0.209	0.178	0.224	0.248	0.402	N/A
w	N/A	0.006	0.51	0	0	1	N/A

Appendix 2.G Material Pre-strained in Equibiaxial tension to 0.20 with 20 minute anneal (EB-20-20) Data and Parameters

Appendix 2.G.1 R^2 values for material pre-strained in Equibiaxial (EB) tension to 0.20 and annealed for 20 minutes at 350 C, at different orientations for different empirical fits: Voce (V), Hollomon (H), Hollomon-Voce (VH), Voce-Line (VL), Voce-Tangent (VT).

Angle from RD (deg)	0	15	30	45	60	75	90
R^2(V)	0.997	0.997	0.998	0.998	0.997	0.968	0.997
R^2(H)	0.993	0.995	0.992	0.993	0.995	N/A	0.992
R^2(VH)	0.997	0.997	0.998	0.998	0.997	0.97	0.997
R^2(VL)	0.997	0.997	0.998	0.998	0.997	0.976	0.997
R^2(VT)	0.997	0.997	0.998	0.998	0.997	0.969	0.997

Appendix 2.G.2 R^2 values in only the post-neck region (pn) for material pre-strained in Equibiaxial (EB) tension to 0.20 and annealed for 20 minutes at 350 C, at different orientations for different empirical fits: Voce (V), Hollomon (H), Hollomon-Voce (VH), Voce-Line (VL), Voce-Tangent (VT).

Angle from RD (deg)	0	15	30	45	60	75	90
R^2(V-pn)	0.621	0.747	0.79	0.795	0.795	N/A	0.792
R^2(H-pn)	N/A	N/A	N/A	N/A	N/A	N/A	N/A
R^2(VH-pn)	0.681	0.742	0.757	0.808	0.823	N/A	0.827
R^2(VL-pn)	0.775	0.772	0.785	0.83	0.817	N/A	0.859
R^2(VT-pn)	0.644	0.802	0.809	0.814	0.901	0.409	0.905

Appendix 2.G.3 Average post-neck (pn) R^2 values for material pre-strained in Equibiaxial (EB) tension to 0.20 and annealed for 20 minutes at 350 C, as well as percent difference with respect to the maximum R^2 value.

	average	% difference
R^2(V-pn)	0.649	14.083
R^2(H-pn)	N/A	N/A
R^2(VH-pn)	0.662	12.251
R^2(VL-pn)	0.691	8.435
R^2(VT-pn)	0.755	0

Appendix 2.G.4 Equibiaxial pre-strain to 0.20 with 20 minute anneal parameters used in Voce (V) model (Eqn. 2.1)

Angle from RD (deg)	0	15	30	45	60	75	90
A	392.727	399.486	375.381	373.709	390.377	357.307	375.454
B	-289.013	-303.52	-267.718	-266.851	-293.865	-272.415	-265.258
C	-7.401	-5.716	-8.8	-8.631	-5.692	-9.393	-8.807

Appendix 2.G.5 Equibiaxial pre-strain to 0.20 with 20 minute anneal parameters used in Hollomon (H) model (Eqn. 2.2)

Angle from RD (deg)	0	15	30	45	60	75	90
K	575.027	571.777	561.848	553.815	548.517	253.046	550.91
N	0.363	0.398	0.331	0.33	0.387	0.181	0.321

Appendix 2.G.6 Equibiaxial pre-strain to 0.20 with 20 minute anneal additional parameters used in Voce-Hollomon (VH) model (Eqn. 2.3)

Angle from RD (deg)	0	15	30	45	60	75	90
α	0.968	0.984	0.888	0.889	0.894	0.5	0.825

Appendix 2.G.7 Equibiaxial pre-strain to 0.20 with 20 minute anneal parameters used in Voce-Linear (VL) model (Eqn. 2.4)

Angle from RD (deg)	0	15	30	45	60	75	90
A'	572.531	432.082	356.239	348.597	365.657	196.199	325.2
B'	-467.333	-335.515	-249.324	-242.781	-269.825	-136.629	-217.499
C'	-6.43	-5.316	-9.408	-9.443	-6.11	-30.273	-10.8
D'	-273.871	-62.3	55.003	70.75	49.654	540.47	146.159

Appendix 2.G.8 Equibiaxial pre-strain to 0.20 with 20 minute anneal additional parameters used in Voce-Tangent (VT) model (Eqn. 2.5)

Angle from RD (deg)	0	15	30	45	60	75	90
ε_n	0.252	0.285	0.221	0.223	0.284	0.231	0.22
w	0.772	0.5	0.693	0.636	0	0	0.35

Appendix 2.H Material Pre-strained in Plane Strain to 0.20 with 20 minute anneal (EB-20-20) Data and Parameters

Appendix 2.H.1 R^2 values for material pre-strained in Plane Strain (PS) to 0.20 and annealed for 20 minutes at 350 C, at different orientations for different empirical fits: Voce (V), Hollomon (H), Hollomon-Voce (VH), Voce-Line (VL), Voce-Tangent (VT).

Angle from RD (deg)	0	15	30	45	60	75	90
R^2(V)	0.996	0.991	0.998	0.997	0.998	0.979	0.919
R^2(H)	0.994	0.989	0.992	0.992	0.992	N/A	N/A
R^2(VH)	0.997	0.991	0.998	0.997	0.998	0.979	0.919
R^2(VL)	0.997	0.991	0.998	0.997	0.998	0.983	0.935
R^2(VT)	0.997	0.991	0.998	0.997	0.998	0.98	0.925

Appendix 2.H.2 R^2 values in only the post-neck region (pn) for material pre-strained in Plane Strain (PS) to 0.20 and annealed for 20 minutes at 350 C, at different orientations for different empirical fits: Voce (V), Hollomon (H), Hollomon-Voce (VH), Voce-Line (VL), Voce-Tangent (VT).

Angle from RD (deg)	0	15	30	45	60	75	90
R^2(V-pn)	0.714	0.662	0.762	0.782	0.748	0.524	N/A
R^2(H-pn)	0.569	N/A	N/A	N/A	N/A	N/A	N/A
R^2(VH-pn)	0.833	0.662	0.75	0.768	0.73	0.8	0.919
R^2(VL-pn)	0.924	0.67	0.756	0.792	0.746	N/A	N/A
R^2(VT-pn)	0.953	0.73	0.789	0.83	0.758	0.701	0.737

Appendix 2.H.3 Average post-neck (pn) R^2 values for material pre-strained in Plane Strain (PS) tension to 0.20 and annealed for 20 minutes at 350 C, as well as percent difference with respect to the maximum R^2 value.

	average	% difference
R^2(V-pn)	0.599	23.736
R^2(H-pn)	0.081	89.659
R^2(VH-pn)	0.78	0.663
R^2(VL-pn)	0.556	29.259
R^2(VT-pn)	0.785	0

Appendix 2.H.4 Plane Strain pre-strain to 0.20 with 20 minute anneal parameters used in Voce (V) model (Eqn. 2.1)

Angle from RD (deg)	0	15	30	45	60	75	90
A	426.996	410.172	386.061	373.66	381.495	370.864	252.655
B	-315.627	-316.734	-277.523	-266.884	-274.015	-281.242	-256.945
C	-6.183	-6.058	-8.593	-8.146	-8.725	-11.233	-32.516

Appendix 2.H.5 Plane Strain pre-strain to 0.20 with 20 minute anneal parameters used in Hollomon (H) model (Eqn. 2.2)

Angle from RD (deg)	0	15	30	45	60	75	90
K	595.934	604.132	575.344	541.618	575.49	290.471	N/A
N	0.363	0.406	0.334	0.329	0.337	0.164	N/A

Appendix 2H.6 Plane Strain pre-strain to 0.20 with 20 minute anneal additional parameters used in Voce-Hollomon (VH) model (Eqn. 2.3)

Angle from RD (deg)	0	15	30	45	60	75	90
α	0.719	0.829	0.909	0.84	0.946	0.99	1

Appendix 2.H.7 Plane Strain pre-strain to 0.20 with 20 minute anneal parameters used in Voce-Linear (VL) model (Eqn. 2.4)

Angle from RD (deg)	0	15	30	45	60	75	90
A'	318.655	329.833	363.239	331.193	382.707	311.857	195.025
B'	-212.314	-239.929	-255.556	-226.458	-275.188	-231.852	-216.806
C'	-9.084	-7.794	-9.281	-9.616	-8.692	-21.626	-51.475
D'	248.451	179.759	64.357	114.353	-3.415	267.577	431.182

Appendix 2.H.8 Plane Strain pre-strain to 0.20 with 20 minute anneal additional parameters used in Voce-Tangent (VT) model (Eqn. 2.5)

Angle from RD (deg)	0	15	30	45	60	75	90
ε_n	0.27	0.28	0.225	0.23	0.223	0.2	0.109
w	0	0	0.59	0.617	0.691	0.247	0

Appendix 2.I Material Pre-strained in Uniaxial tension to 0.20 with 20 minute anneal (EB-20-20) Data and Parameters

Appendix 2.I.1 R^2 values for material pre-strained in Uniaxial (UA) tension to 0.20 and annealed for 20 minutes at 350 C, at different orientations for different empirical fits: Voce (V), Hollomon (H), Hollomon-Voce (VH), Voce-Line (VL), Voce-Tangent (VT).

Angle from RD (deg)	0	15	30	45	60	75	90
R^2(V)	0.996	0.993	0.978	0.98	0.981	0.978	0.995
R^2(H)	0.99	0.983	N/A	N/A	N/A	N/A	0.988
R^2(VH)	0.996	0.994	0.978	0.98	0.981	0.978	0.995
R^2(VL)	0.996	0.996	0.986	0.987	0.988	0.985	0.995
R^2(VT)	0.996	0.996	0.979	0.981	0.982	0.979	0.995

Appendix 2.I.2 R^2 values in only the post-neck region (pn) for material pre-strained in Uniaxial (UA) tension to 0.20 and annealed for 20 minutes at 350 C, at different orientations for different empirical fits: Voce (V), Hollomon (H), Hollomon-Voce (VH), Voce-Line (VL), Voce-Tangent (VT).

Angle from RD (deg)	0	15	30	45	60	75	90
R^2(V-pn)	0.749	0.66	0.334	0.63	0.61	0.584	0.859
R^2(H-pn)	N/A	N/A	N/A	N/A	N/A	N/A	N/A
R^2(VH-pn)	0.747	0.788	0.336	0.645	0.62	0.583	0.829
R^2(VL-pn)	0.747	0.944	N/A	N/A	N/A	N/A	0.742
R^2(VT-pn)	0.775	0.961	0.705	0.911	0.891	0.848	0.865

Appendix 2.I.3 Average post-neck (pn) R^2 values for material pre-strained in Uniaxial (UA) tension to 0.20 and annealed for 20 minutes at 350 C, as well as percent difference with respect to the maximum R^2 value.

Angle from RD (deg)	Average	% difference
R^2(V-pn)	0.632	25.694
R^2(H-pn)	N/A	N/A
R^2(VH-pn)	0.65	23.628
R^2(VL-pn)	0.347	59.16
R^2(VT-pn)	0.851	0

Appendix 2.I.4 Uniaxial pre-strain to 0.20 with 20 minute anneal parameters used in Voce (V) model (Eqn. 2.1)

Angle from RD (deg)	0	15	30	45	60	75	90
A	366.531	406.672	354.346	360.196	358.715	356.341	429.25
B	-263.91	-333.538	-274.26	-276.757	-274.978	-274.335	-341.867
C	-8.846	-6.914	-11.547	-10.483	-10.846	-11.631	-5.253

Appendix 2.I.5 Uniaxial pre-strain to 0.20 with 20 minute anneal parameters used in Hollomon (H) model (Eqn. 2.2)

Angle from RD (deg)	0	15	30	45	60	75	90
K	553.797	626.931	275.328	270.084	275.702	279.489	615.339
N	0.336	0.42	0.166	0.163	0.165	0.165	0.431

Appendix 2.I.6 Uniaxial pre-strain to 0.20 with 20 minute anneal additional parameters used in Voce-Hollomon (VH) model (Eqn. 2.3)

Angle from RD (deg)	0	15	30	45	60	75	90
α	0.966	0.823	0.999	0.946	0.953	0.986	1

Appendix 2.I.7 Uniaxial pre-strain to 0.20 with 20 minute anneal parameters used in Voce-Linear (VL) model (Eqn. 2.4)

Angle from RD (deg)	0	15	30	45	60	75	90
A'	361.26	290.528	282.642	268.655	273.34	283.221	714.278
B'	-258.826	-238.349	-212.838	-196.502	-198.232	-211.637	-622.797
C'	-9.026	-11.413	-29.443	-23.547	-24.04	-27.682	-3.364
D'	15.967	273.423	328.878	339.625	334.702	328.447	-429.602

Appendix 2.I.8 Uniaxial pre-strain to 0.20 with 20 minute anneal additional parameters used in Voce-Tangent (VT) model (Eqn. 2.5)

Angle from RD (deg)	0	15	30	45	60	75	90
ε_n	0.221	0.271	0.2	0.21	0.207	0.199	0.306
w	0.531	0.013	0.396	0.229	0.157	0.383	0.765

CHAPTER 3

ANISOTROPIC BEHAVIOR OF ALUMINUM ALLOY 5182 SUBJECT TO PREFORM ANNEALING

ABSTRACT

Investigation was conducted into the effects of pre-strain and annealing on the anisotropy of Aluminum AA5182-O as characterized by the R-value. The robustness of the digital image correlation method was verified and has replaced the use of extensometers in this research. The dependence of R-value on the direction of uniaxial testing was correlated with pre-strain and annealing, revealing strain-path as well as strain-path angle to be useful tools in predicting the strain-paths that yield the greatest isotropy in the material. Additionally, the time-dependent effect of annealing on material anisotropy was determined to be coupled with strain-path. Electron backscatter diffraction analysis was used to obtain texture data, revealing textural evolution corresponding to the R-values observed.

3.1 INTRODUCTION

"Preform annealing" [Krajewski, 2007] is a forming technique developed to improve the formability of aluminum alloys at room temperature through a two-stage forming with intermediate annealing. Annealing partially or completely removes the effects of cold work from the preform and recovers material ductility for the sake of fabricating a complex aluminum shape in the 2nd-stage forming, at the level of conventional steel shapes. An issue is that limited research has been reported on the anisotropy of the material that is subjected to strain path change (preform) and annealing treatment.

The anisotropy of a material represents its response to straining in different directions. Of particular importance is the planar anisotropy describing the difference between the properties in the plane of the sheet and those in the through-thickness direction. This must usually be taken into account during typical sheet metal forming procedures. The planar anisotropy is quantified by a parameter known as the R-value, which plays an important role in Hill's yield criteria for generally anisotropic metals [Hill, 1948] as well as orthotropic metals [Hill, 1993] such as aluminum alloy ~~-~~5182-O.

Essentially, the R-value is defined as the incremental width strain divided by the incremental thickness strain that a material experiences in response to uniaxial straining [Lankford~~,~~ et al., 1950]. Consequently, R-values are strongly dependent on the direction of straining and strain increments [Rees, 1997]. This makes experimental determination of R-values difficult as it is very error prone and time consuming to measure width strain with traditional techniques such as extensometers [Liu, 1985]. Furthermore, limited research has been conducted on how these R-values evolve as a result of both pre-straining and annealing. Annealing removes cold work in a material partially or entirely by reducing dislocation density through annihilation or by altering its microstructure. The latter can have a significant effect on the R-values, anisotropy, and formability of metals such as aluminum. As annealing is a key step in the pre-form annealing method, it is useful to create a more general scheme for assessing the impact of these factors on material anisotropy.

Thus, this research uses an advanced experimental technique, digital image correlation (DIC) for strain measurement, in determining R-values after uniaxial tension tests performed on materials that have been subjected to pre-straining and annealing. Additionally, this research links the effect of pre-straining with texture evolution in the material. Lastly, it proposes a simple method for combining the effect of pre-strain and annealing on R-values by examining the correlation between the effective strain path of the material and its resulting anisotropy.

3.2 MATERIALS, EXPERIMENTAL AND ANALYTICAL PROCEDURE

3.2.1. Material

The material is commercial aluminum alloy 5182-O with 1.1 mm nominal thickness. Its chemical composition is reported in Table 3.1. The average grain diameter in the rolling plane is around 15 μm, measured by electron backscatter diffraction (EBSD) analysis. The crystallographic texture of the as-received (AR) material is summarized in Figure 3.1, where the (001), (011) and (111) pole figures included in Figures 3.1a and 3.2b describes the orientation distribution function (ODF) expressed by Euler angles, ϕ_1, Φ, and ϕ_2. Both Figures 3.2a and b indicate that the AR material has a weak texture, mainly the recrystallization Cube component {100}<001> and retained deformation Brass component {110}<112>.

Table 3.1. Chemical composition of AA5182-O (wt %)

Al	Mg	Mn	Fe	Si	Cu	Ni	Ti	Zn
Bal	4.3	0.34	0.21	0.03	<0.01	<0.01	<0.01	<0.01

3.2.2. Pre-straining, Annealing and Tensile Tests

To measure the effect of process variables on anisotropy, the material was subjected to various pre-straining and annealing conditions and tested in uniaxial tension on an Instron tensile machine, where load and strain data were recorded by the DIC system.

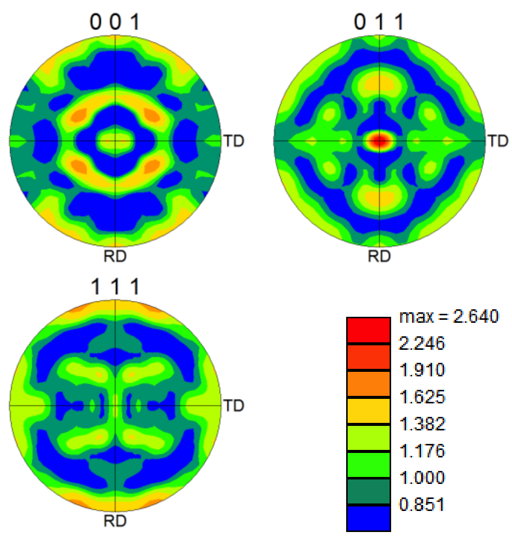

(a)

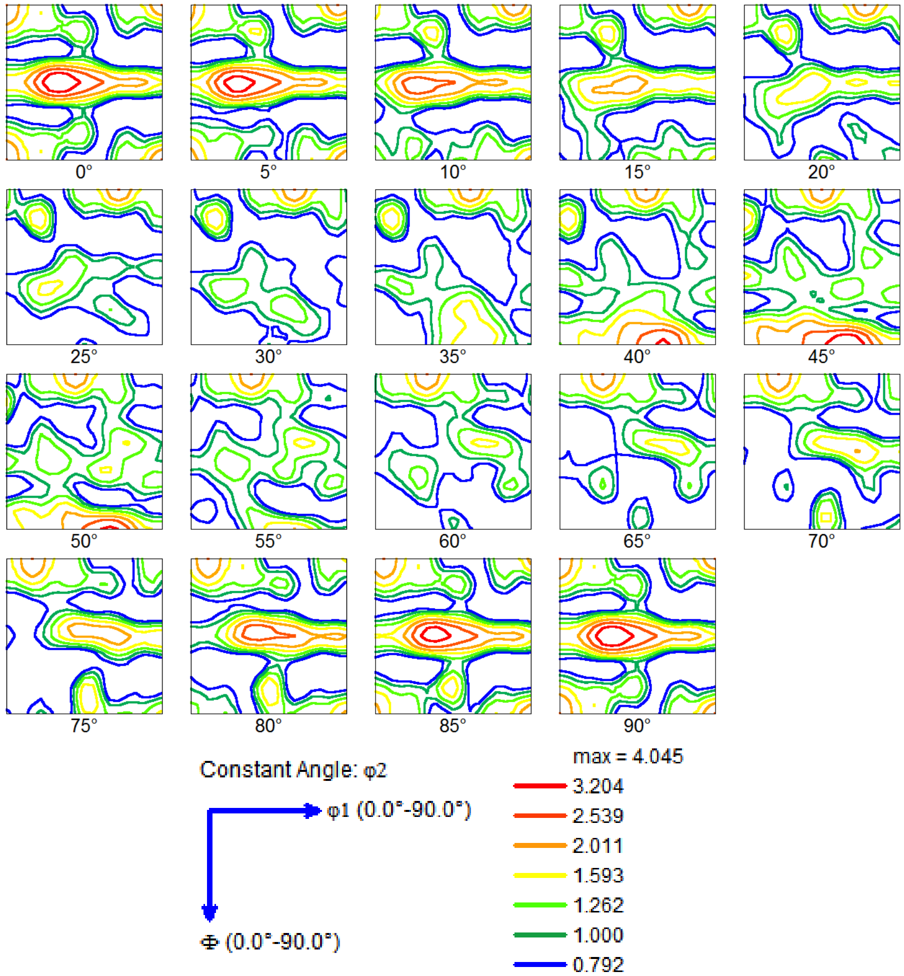

(b)

Figure 3.1 Texture of as-received AA5182-O: (a) (001), (011) and (111) pole figures; and (b) ODF

Pre-straining and Annealing

The materials that were pre-strained were cut from large tensile specimens loaded in the transverse direction (TD). By controlling the clamping geometry of these materials, it was possible to obtain three different types of strain paths: equibiaxial, plane strain, and uniaxial (further details can be found in [Li et al., 2011]). The materials were pre-strained to 0.20 for each of these strain paths, with an additional group of specimens pre-strained to 0.15 in uniaxial tension. After tensile specimens were extracted from each sheet, some of them were annealed in a salt bath at 350 °C for 10 ~~-~~seconds and 20 ~~-~~minutes in anticipation of triggering different microstructural changes (further details can be found in [Li et al., 2011].

Conducting Uniaxial Tension Tests and Strain Measurement via DIC

In preparation for testing, a speckle pattern was applied to each tensile specimen so that its deformation could be tracked in three dimensions by the DIC system. The specimens were then tested in uniaxial tension, under ambient conditions at 5 mm/min where strain and load data were recorded via the DIC system and Instron tensile testing machine.

3.2.3. EBSD procedure

EBSD studies were performed on the AR specimens and specimens pre-strained to 0.20 in equibiaxial tension with no anneal (hereafter referred to as EB-20-0). The EBSD specimens were prepared by cutting with a low speed precision diamond saw. The EBSD surface was mechanically polished with progressively finer water based diamond suspensions (down to 1.0 µm) and then polished by 0.05 µm colloidal silica. The EBSD data were acquired using a CARL ZEISS SEM through a HKL Channel-5 camera. For statistical robustness, the scanned area included at least 800 grains at a high spatial resolution (with a step size of 3 μm or lower). The Tex-SEM Ltd (TSL) analysis software was used for routine texture analysis of the EBSD data. This included measurement of grain size and distribution, GAM values, pole figures and ODF for the as-received and pre-strained material.

3.2.4. Analytical Procedure

Anisotropy

Metallic through-thickness anisotropy is characterized by a parameter known as the Lankford coefficient, or R-value, the ratio of plastic width strain rate to plastic thickness strain -rate. Often, an approximation of this quantity is used instead; this is known as the average R-value (the ratio of total plastic width strain to total plastic thickness strain) denoted here as R_m:

$$R_m = \left[\frac{\varepsilon_{xx}}{\varepsilon_{zz}}\right]_{plastic} \tag{3.1}$$

Here ε_{xx} refers to the true plastic width-strain and ε_{zz} refers to the true plastic thickness-strain. However, the original quantity contemplated in Hill's model is the strain-rate based instantaneous R-value, known as R_H [Liu, 1985]. As this quantity captures the normal anisotropy of the material at a given instant, it is in fact R_H that is the true material property. It is defined as follows:

$$R_H = \left[\frac{\frac{d\varepsilon_{xx}}{dt}}{\frac{d\varepsilon_{zz}}{dt}}\right]_{plastic} \tag{3.2}$$

which can be written as:

$$R_H = \left[\frac{\frac{d\varepsilon_{xx}}{dt}}{-\left(\frac{d\varepsilon_{xx}}{dt}+\frac{d\varepsilon_{yy}}{dt}\right)}\right]_{plastic} \tag{3.3}$$

Note that the above equation makes the traditional assumption of volume conservation during plastic deformation to express the thickness strain, ε_{zz}, in terms of both the width strain, ε_{xx}, and longitudinal strain, ε_{yy}. If R_H is known at different orientations for a particular sample, it is useful to consider an average value of R_H across these orientations.

This average R-value ($\bar{R}$) is often used to characterize the resistance against thinning; it is defined as

$$\bar{R} = \frac{R_0+2R_{45}+R_{90}}{4} \tag{3.4}$$

where the suffix indicates the direction in which R-value is measured from the RD, where R_0, R_{45} and R_{90} denote R-values in the rolling, diagonal and transverse directions, respectively. If seven individual R_H values are measured at different orientations ranging from 0 to 90 degrees in 15 degree increments from the RD, then $\bar{R}$ becomes [Hamada and Inoue, 2010]

$$\bar{R} = \frac{R_0+2(R_{15}+R_{30}+R_{45}+R_{60}+R_{75})+R_{90}}{12} \tag{3.5}$$

Data Extraction from DIC Output

The actual raw data collected is the sequence of images of the surface of the deforming specimens using two synchronized cameras. This tracking system provided a 3D displacement contour map of the entire deformation process up to the onset of fracture. The true strain fields and true strain-rate fields were subsequently calculated from DIC post-processing of the images. The elastic contribution to the strains and strain-rates were also eliminated in post-processing via load information.

It was observed, however, that the strain-rates themselves were not useful in calculating R-values for specimens because of the extreme fluctuations they displayed over short time intervals in the DIC output, due to the derivative amplification of the phenomenon of serrated flow. Nevertheless, the expression for R_H may be easily transformed into a time independent function by observing that $\frac{d\varepsilon_{yy}}{dt}$ factors out of the volume-conserved expression for R_H:

$$R_H = \left[\frac{\frac{d\varepsilon_{xx}}{d\varepsilon_{yy}}\frac{d\varepsilon_{yy}}{dt}}{-\left(\frac{d\varepsilon_{xx}}{d\varepsilon_{yy}}\frac{d\varepsilon_{yy}}{dt}+\frac{d\varepsilon_{yy}}{dt}\right)}\right]_{plastic} \tag{3.6}$$

Yielding:

$$R_H = \left[\frac{\frac{d\varepsilon_{xx}}{d\varepsilon_{yy}}}{-\left(\frac{d\varepsilon_{xx}}{d\varepsilon_{yy}}+1\right)}\right]_{plastic} \tag{3.7}$$

The advantage of this reformulation is that a preemptive linear fitting can be done between ε_{xx} as a function of ε_{yy}, resulting in a constant value for $\frac{d\varepsilon_{xx}}{d\varepsilon_{yy}}$. Consequently, the serration associated with direct measurement of strain-rate may be eliminated and a constant value for R_H may be obtained [Liu and Zhu, 1995]. Thus, this time-independent method was the procedure used to determine R-values for all the specimens examined. Note that the linear fitting between ε_{xx} and ε_{yy} was restricted to data from the yield strain to necking strain, as this is the region where the R-value is normally defined.

Deformation Due to Pre-strain

For a given pre-strain, the principal strains are functions of the pre-strain level. By assuming that (a) the material was isotropic and (b) the material volume remained constant during plastic deformation, the formula for the principal strains (ε_1, ε_2, and ε_3) and equivalent strain ($\bar{\varepsilon}$) is

$$\bar{\varepsilon} = \sqrt{\frac{2}{3}(\varepsilon_1^2 + \varepsilon_2^2 + \varepsilon_3^2)} \tag{3.8}$$

When the specimen is pre-strained along the transverse or rolling direction (in the current research, the material is stretched along the TD) and no shear strain is introduced, the strains in TD and RD are the major and minor strains, respectively. Thus, Eq. (3.6) can be written as

$$\bar{\varepsilon} = \sqrt{\frac{2}{3}(\varepsilon_{TD}^2 + \varepsilon_{RD}^2 + \varepsilon_{zz}^2)} \tag{3.9}$$

where ε_{TD}, ε_{RD}, and ε_{zz} are the true strains along TD, RD, and normal (zz) directions of the aluminum sheet. For different pre-strain paths, the formulas to calculate the pre-strain levels are summarized in Table 3.2.

Table 3.2 the formulas for the calculation of the pre-strain levels

Pre-strain path	Major Strain ε_1 (i.e.ε_{TD})	Minor Strain ε_2 (i.e.ε_{RD})
Uniaxial tension	$\varepsilon_{TD} = \bar{\varepsilon}$	$\varepsilon_{RD} = -\frac{\bar{\varepsilon}}{2}$
Plane strain	$\varepsilon_{TD} = \frac{\sqrt{3}}{2}\bar{\varepsilon}$	0
Equibiaxial tension	$\varepsilon_{TD} = \frac{\bar{\varepsilon}}{2}$	$\varepsilon_{RD} = \frac{\bar{\varepsilon}}{2}$

The equivalent plastic strain (EPS) method [Li et al., 2013] was applied to evaluate the equivalent strain that remained in the material after annealing for the fact that the annealing treatment relieved stored cold work in the material, effectively reducing the pre-strain level. Thus, for specimens that have undergone annealing, the values of ε_{TD} and ε_{RD} will be reduced. The extent of resetting increases with annealing time for a set annealing temperature (the case of the current research). For materials pre-strained to 0.20, the corresponding value of $\bar{\varepsilon}$ is 0.18 for no anneal (due to relaxation after unloading), 0.08 for a 10 second anneal, and -0.007 for a 20 minute anneal (due to further softening of the material with grain growth).

Combining Pre-strain and Strain in Testing

In order to express correlations between the total deformation history of a specimen and its R-value, it is important to express the testing deformation in the same coordinate system as the deformation caused by pre-straining, namely the rolling and transverse directions (RD and TD, respectively). For this two-stage forming, in order to ultimately express all deformation in the same coordinate system, it is necessary to introduce two coordinate systems: the pre-strain basis and testing basis. Since the pre-strain was applied along the specimen TD, the pre-strain coordinate system refers to the directions defined by RD and TD, (as mentioned in Eq. 3.7); these are the specimen's original coordinates. The testing coordinate system refers to the *x* and *y* directions of the tensile test (where *x* refers to the width direction and y refers to the longitudinal direction). Thus, the testing deformation, which is in the x-y coordinate system, can be transformed to the pre-strain or specimen coordinate system, based in RD and TD.

For any given specimen subjected to one particular pre-strain (including path and level), the coordinate system describing the path of this pre-strain will be common with like specimens; however, as these specimens will be tested in different orientations, it will have an individual testing coordinate system (corresponding to its particular pulling direction ranging from 0 to 90 degrees in 15 degree increments from the RD in the uniaxial tests). Indeed, the specimen orientation θ is related to the angular transformation (2θ) used in Mohr's circle, which can be used to convert strains calculated in the specimen's testing direction to their corresponding values in the pre-strain -coordinate system, defined by the original RD and TD directions.

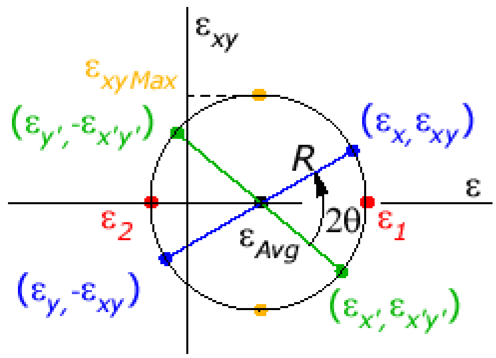

Figure 3.2 An illustration of transforming strains by an angle θ from one coordinate system, the unprimed system, to another coordinate system, the primed system. In this case, the unprimed system represents the testing coordinate system; the primed system represents the specimen's original coordinate system defined by RD and TD. In this diagram, from [http://www.efunda.com/formulae/solid_mechanics/mat_mechanics/mohr_circle_usage_strain.cfm], ε_i is shorthand for ε_{ii}, the diagonal components of the strain tensor.

Like stress, strain can be represented as a symmetric second-order tensor. For an in-plane state of strain, i.e. the *x-y* plane, the strain axis rotation (from the x-y plane to the x'-y' plane) is governed by

$$\begin{aligned} \varepsilon'_{xx} &= \varepsilon_{xx}\cos^2\theta + \varepsilon_{yy}\sin^2\theta + 2\gamma_{xy}\sin\theta\cos\theta \\ \varepsilon'_{yy} &= \varepsilon_{yy}\cos^2\theta + \varepsilon_{xx}\sin^2\theta - 2\gamma_{xy}\sin\theta\cos\theta \\ \gamma'_{xy} &= (\varepsilon_{yy} - \varepsilon_{xx})\sin\theta\cos\theta + \gamma_{xy}(\cos^2\theta - \sin^2\theta) \end{aligned} \tag{3.10}$$

where ε_{xx} and ε_{yy} refer to the normal strains and γ_{xy} is the shear strain in the unprimed, i.e. testing coordinate system; ε'_{xx} and ε'_{yy} refer to the normal strains and γ'_{xy} is the shear strain in the primed, i.e. specimen coordinate system. Here θ represents the axis rotation from the unprimed, testing coordinate system to the primed, specimen coordinate system. The purpose of using this transformation is to view the effects of the uniaxial tension test (after pre-straining), which is performed at different orientations with respect to the pre-strain coordinate system. Thus, the contribution to the total strain due to pre-strain before tensile testing is able to be incorporated into this framework.

In other words, although ε_{xx} and ε_{yy} cannot be additively combined with ε_{TD} and ε_{RD} (the pre-strains in Eq. 3.7), after a coordinate transformation into the pre-strain coordinate system, ε'_{xx} and ε'_{yy} can be added with ε_{TD} and ε_{RD} directly. Therefore, another quantity θ' may be considered, where θ' represents the total strain-path angle as measured from the RD:

$$\theta' = \tan^{-1}\frac{\varepsilon'_{xx}+\varepsilon_{TD}}{\varepsilon'_{yy}+\varepsilon_{RD}} \tag{3.11}$$

3.3 RESULTS AND DISCUSSION

3.3.1. As-Received and Pre-strain without annealing

The microstructure and texture of the AR and EB-20-0 pre-strained specimens were compared revealing that the average grain size was slightly reduced from 15 to 13 µm. Figure 3.4 summarizes the texture development, including pole figures (Figure 3.3a) and ODF (Figure 3.3b). It is noticed that the Brass texture becomes stronger compared to the

AR material (Figure 3.1). The development of a (110)-fiber ($\varphi_1 = 0$ to 35 deg, $\Phi = 45$ deg, and $\varphi_2 = 45$ deg) is the most prominent result of the equibiaxial stretch [Hu et al., 2012].

The instantaneous R-values are plotted as functions of the angle from RD for AR, equibiaxial (EB), plane strain (PS), and uniaxial (UA) pre-strained specimens (Figure 3.4), where the pre-strain directions for PS and UA are along the TD and pre-strain levels are 0.2, 0.2, 0.15 equivalent true, respectively. These pre-strained specimens, denoted by their path and pre-strain level as EB-20, PS-20, and UA-15 were not annealed. Due to the testing conditions, uniaxial pre-strain to 0.20 was missing; instead UA-15 is presented here to provide some information on the effects of uniaxial pre-strain. It was found that the R-value remains constant during deformation if there is no strain path change [Huang et al., 2011] because of the fact that the texture becomes sharper with increasing strain but no texture orientation changes. Therefore, the R-values of UA-15 should be able to provide insight into the anisotropy of specimens that would have been pre-strained in uniaxial tension to 0.2.

The texture results explain the R-value changes to some extent. The stronger {110}<112> (Brass) texture developed in EB pre-strain results in the anisotropic R-values, which are higher at the direction of 45 degrees with respect to the RD but lower at the directions of 0 and 90 degrees. The R-values of PS-20 specimens have a similar trend with orientation angles, but are lower compared to AR material. The UA-15 pre-strained specimens show an increasing trend in R-values from 0 to 90 degrees but R_{45} is relatively high and forms a small peak in the middle. Further texture analysis is needed for PS and UA pre-strain paths.

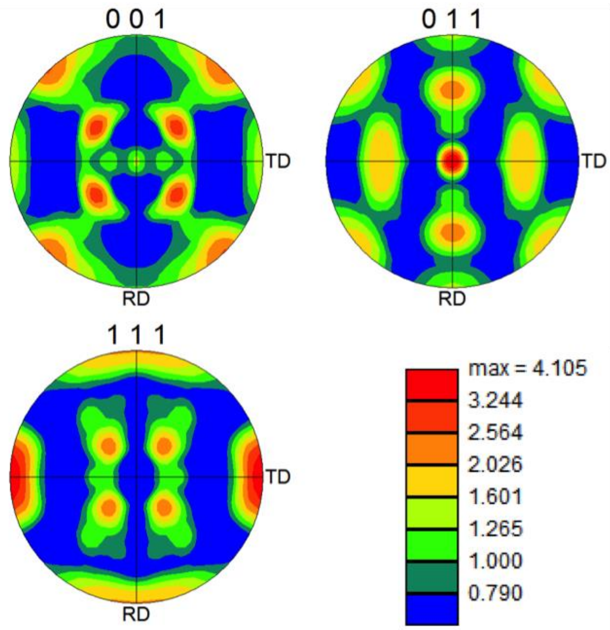

(a)

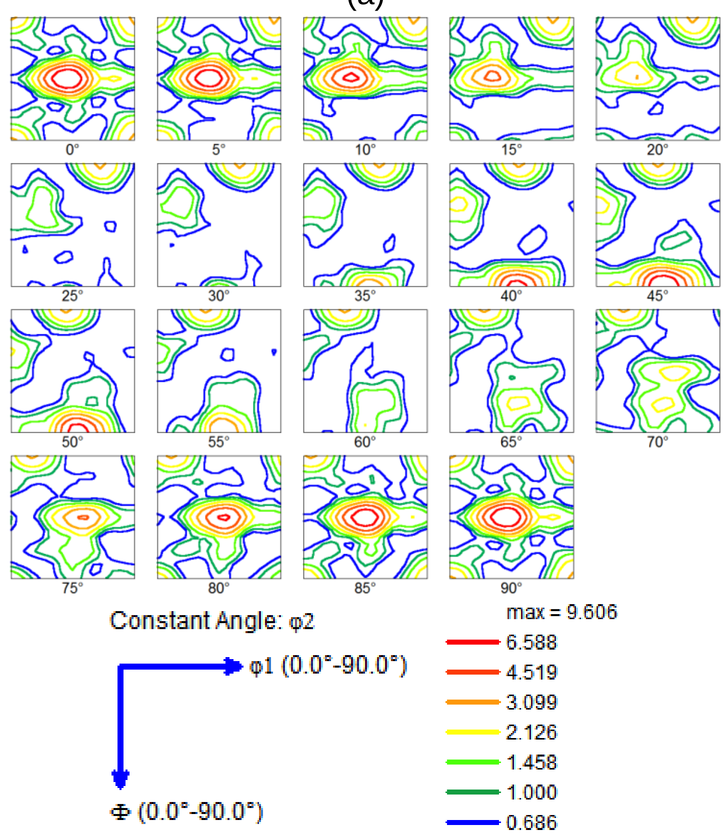

(b)

Figure 3.4 Texture of 0.2 EB pre-strained AA5182-O: (a) (001), (011) and (111) pole figures; and (b) ODF

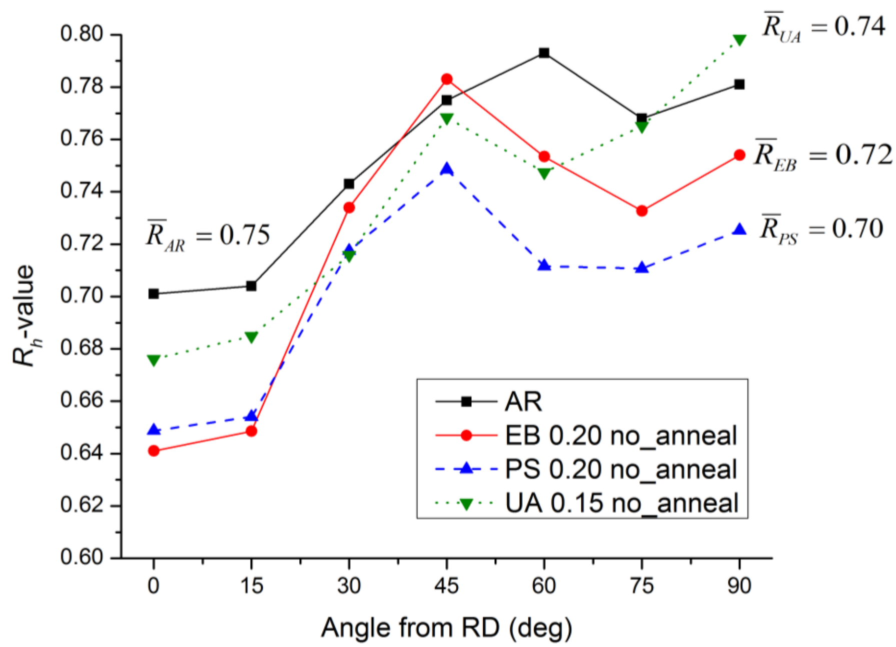

Figure 3.5 R-values plots as a function of angle to RD for AR and EB 0.2, PS 0.2 and UA 0.15 pre-strained specimens, without annealing

The average $\bar{R}$-values are also summarized in Figure 3.5. $\bar{R}$ of less than one means that the sheet material has undergone more through-thickness than in-plane deformation. A higher $\bar{R}$ indicates a better formability of the sheet metal because it is more resistant to thinning. After pre-straining, $\bar{R}$ was reduced for all three pre-strained paths, especially the PS pre-strain. This is expected since the Chapter 2 analysis showed that the pre-strained specimens have a lower formability than AR material.

The magnitude and direction of the strain path changed during the two-stage deformation process (pre-straining and tensile testing). An example is given in Figure 3.6, where the AR specimens were first pre-strained along EB, PS and UA for 0.2, 0.2 and 0.15 equivalent true strains, respectively, and then tested in uniaxial tension along TD and RD until fracture where the strains were recorded up to necking. This strain path angle, θ', defined by Eq 3.11 is the angle from the RD to the final strain stage, as shown in Figure 3.6. Besides these two uniaxial testing directions, the pre-strained specimens were tested from 15 to 75 degrees in 15-degree increments from the RD. The analysis becomes more complex when more orientations were involved. To investigate how the changes in strain path influence the R-values, a new diagram with strain path angle (θ') is proposed, as shown in Figure 3.7, where the R-values are plotted as functions of strain path angle; the seven data points on each curve present the seven orientations in the uniaxial tensile tests (from 0 to 90 degrees, with 15-degree increments from RD); and the 1st quadrant region (i.e. θ' = 0 ~ 90 degrees) corresponds to the 1st quadrant in Figure 3.6, and so forth with the 2nd and 4th quadrants. Compared to pre-strained specimens, AR specimens have higher R-values (indicating greater isotropy) and a wider range of strain path angles; EB pre-strains narrow the final strain path within the 1st quadrant; PS pre-strains are in the middle and produce relatively lower R-values

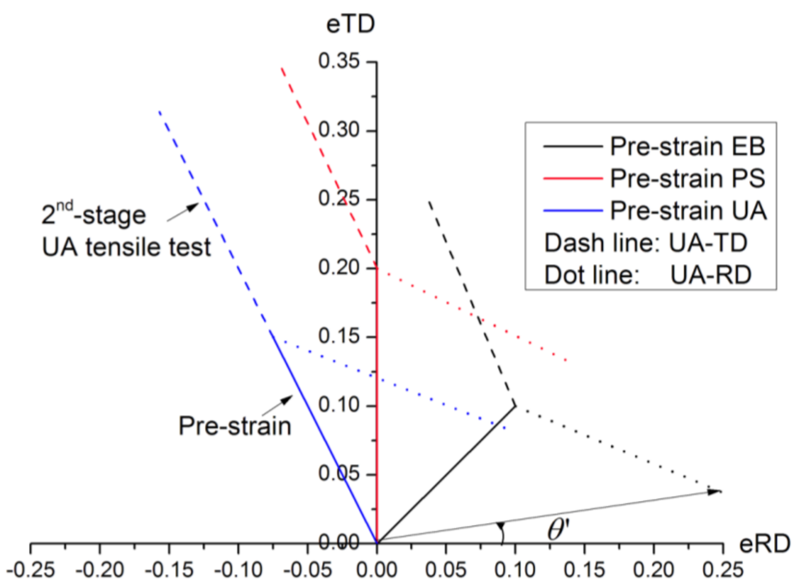

Figure 3.6 Strain paths for pre-strain and 2nd-stage uniaxial tensile tests: pre-strains are along three directions, EB 0.2. PS 0.2 and UA 0.15. No further annealing conducted. Two strain paths are plotted in the 2nd-stage uniaxial tensile tests, i.e. 90 degrees (dashed) and 0 degrees (dotted).

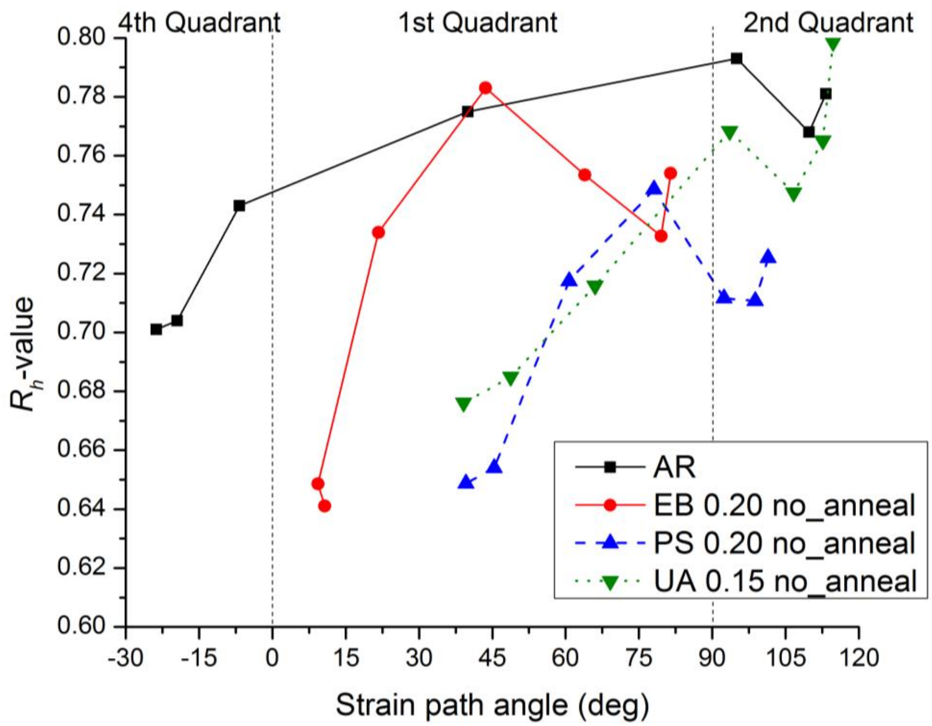

Figure 3.7 R-values plots as a function of strain path angle for AR and EB 0.2, PS 0.2 and UA 0.15 pre-strained specimens, without further annealing

(indicating greater anisotropy); UA pre-strains tend to take the final strain path towards the 2nd quadrant. This is a result of the direction of the pre-strain path, as indicated in Figure 3.6, where the EB strains place the start of the testing deformation in the 1st quadrant, PS lies in division between the 1st and 2nd quadrant, and UA lies in the 2nd quadrant. Information regarding pre-strain path effects are not seen in Figure 3.5 (the traditional R-value plotting method [Kocks et al., 2000]), but is included by considering the strain path angle. This information will be useful in the future analysis in conjunction with EBSD texture evolution data.

To further illustrate the benefits of strain path angle method, consider the as-received material in Figure 3.5. For convenience, the actual R-values are tabulated below.

The traditional method, illustrated by this figure, simply plots R-value as a function of the orientation of the tensile test. It is not readily apparent from this plot why R_{60} should be the highest R-value. However, the strain path diagram in Figure 3.8 illustrates the reason. The 60° direction results in a strain path close to the vertical (with a strain path angle $\theta' = 94.977$ degrees, Table 3.3). Thus, this vertical strain path counteracts the anisotropy introduced into the AR material due to the rolling process itself.

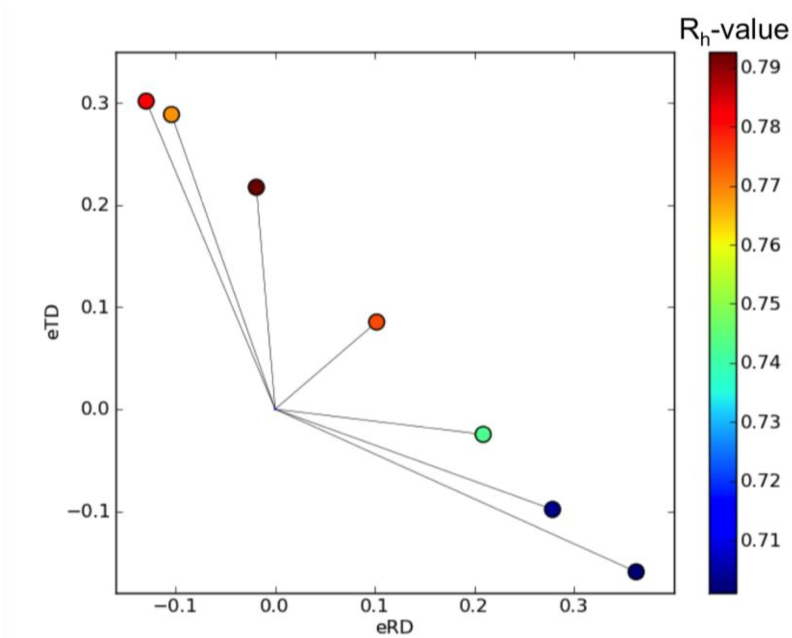

Figure 3.8 As-received strain paths in the pre-strain basis (defined by εRD and εTD). The gray lines indicate the strain paths taken by individual uniaxial tension tests, with color indicating the final R-value.

Table 3.3 As-received R-values, denoted as R_h, as a function of testing direction measured from the rolling direction (RD) and as function of the strain path angle θ'.

Angle from RD (deg)	0	15	30	45	60	75	90
θ'	-23.497	-19.461	-6.764	39.995	94.977	109.811	113.205
R_h	0.701	0.704	0.743	0.775	0.793	0.768	0.781

3.3.2. Pre-strain with annealing

The effects of pre-strain and annealing on the instantaneous R-values are summarized in Figure 3.9, where two pre-strain paths (EB and PS) are included; three heat treatments are involved (no anneal, annealing at 350°C for 10 seconds and 20 minutes); AR materials are used as control specimens. It was noticed that the recovery dominates during 10-second annealing and recrystallization occurs when the annealing time is extended to 20 minutes [Li et al., 2011]. The recovery reduces the dislocation density and will not cause significant crystal orientation change; however, the recrystallization will generate new crystal structures and thus change the orientation. This is reflected by the R-values of the annealed specimens. Nevertheless, compared to the specimens pre-strained with no further annealing treatment, the 10-second annealed specimens have higher R-values; both PS and EB pre-strained specimens still have the highest R-values at 45 degrees from RD; and the position of the R-value curve from the PS pre-strained specimens is still on the right of the EB pre-strained specimens.

However, for the 20-minute anneal, except for the few significant increases in R-values, the R-value curve of PS pre-strained specimens is above the EB pre-strained specimens, which means annealing for a longer time (triggering recrystallization) mitigates the pre-strain path effect on strain path angles or final strain stages in the tensile specimens. This may be due to the introduced random texture after 20-minute annealing. Further EBSD analysis is needed to confirm this hypothesis.

The effect of annealing on strain path and R-values can be visualized by looking at the pre-strain path and EPS taken in the pre-strain coordinate system. Figures 3.10 (a-c) summarize the examples on 0.2 EB pre-strained specimens for no anneal, annealing at 350°C for 10 seconds and 20 minutes conditions, respectively, where the blue arrow indicates the EPS direction and value after pre-strain and annealing; the gray line shows the strain paths taken by individual uniaxial tension tests, with color indicating the R-values.

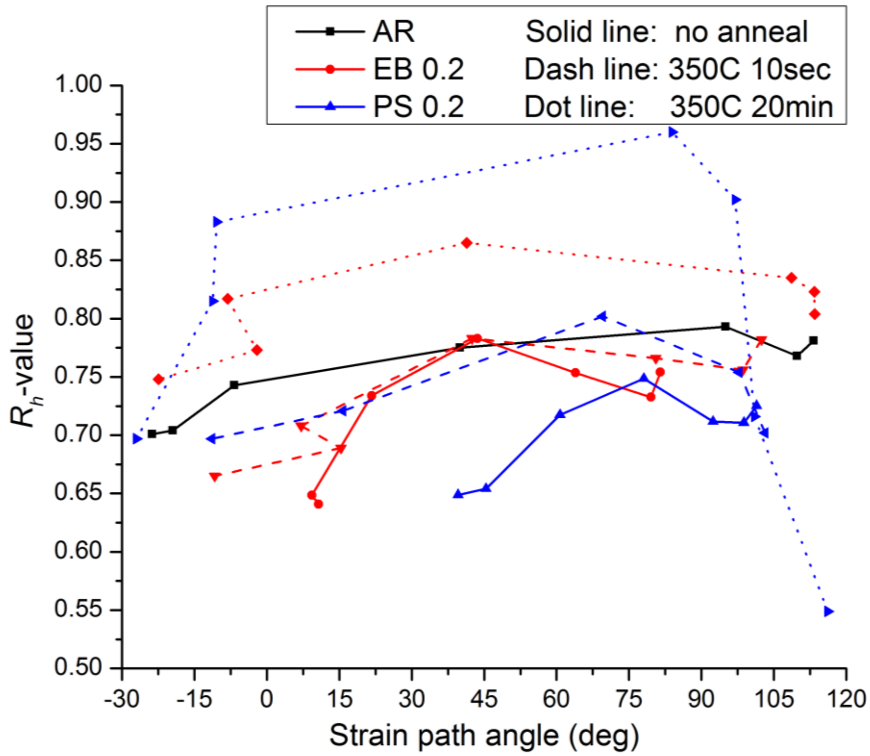

Figure 3.9 R-value plots as a function of strain path angle for AR, EB 0.2 and PS 0.2, where three heat treatments involved: no anneal (solid), annealed at 350°C for 10 seconds (dashed) and 20 minutes (dotted).

Annealing for 10 seconds or 20 minutes increases the R-values for all the testing directions. The impact of annealing can also be quantified through the reduction of the magnitude of the initial pre-strain vector, indicated by the value of EPS. Because 10-second annealing is not long enough to trigger recrystallization, the material has become softer through only decreases of dislocation densities and thus may not experience significant texture evolution. This is reflected by the strain path diagram by the fact that the asymmetry of the R-values about the diagonal is still present in Figure 3.10b. Longer annealing of 20 minutes, however, may generate random texture and cause the material to be more isotropic. This can be seen in Figure 3.10c, where the R-values overall are greater, and more symmetric about the 45 degree diagonal strain path.

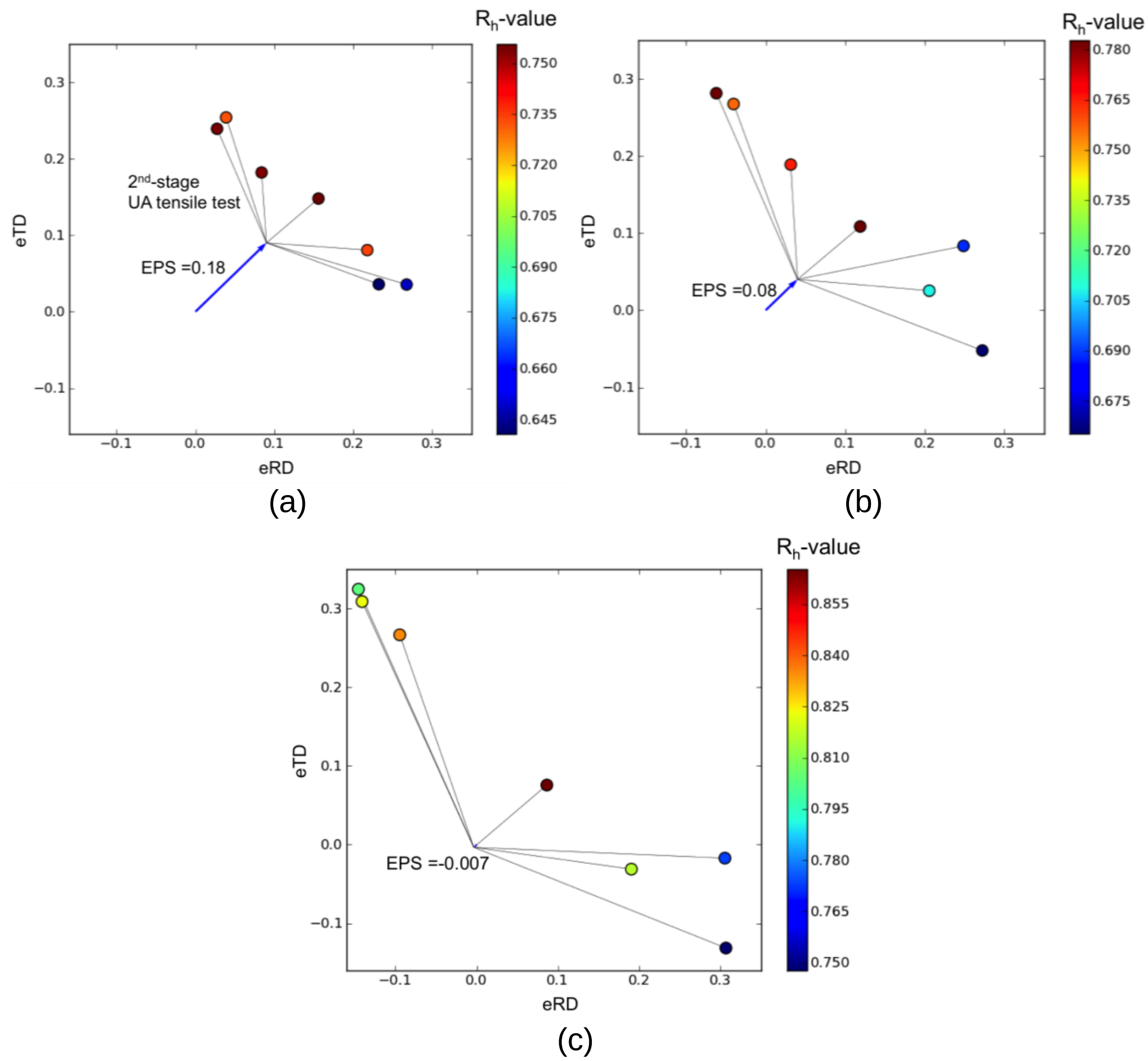

Figure 3.10 R_h-values of 0.2 EB pre-strained and annealed specimens plotted in the pre-strain coordinate system (defined by eRD and eTD). The blue arrow indicates the EPS after initial equibiaxial pre-straining and annealing, starting at (eRD, eTD) = (0,0); The gray lines indicate the strain paths taken by individual uniaxial tension tests, with color indicating the R-value. (a) no anneal, (b) annealed at 350°C for 10 seconds and (c) annealed at 350°C for 20 minutes.

As can be seen from Figures 3.10 b and c, the strain paths leave the 1st Quadrant (corresponding to positive eRD and eTD) for the 10-second and 20-minute anneals due to reaching a higher strain during the uniaxial tension test as a consequence of softening after annealing. Yet, while the R-values and thus isotropy is increased for all testing directions after annealing, the final R-values are still not symmetric about the 45 degree direction, indicating that the heat treatment does not eliminate all the initial in-plane anisotropy of the AR material. It is however more isotropic overall. Further details regarding other strain paths can be found in the Appendix.

3.4 CONCLUSIONS

R-value, which is closely tied with formability, has a strong correlation with strain path. The strain path is determined from the resultant strains of the uniaxial tensile test, the testing direction, the pre-strain level and path, and the annealing time. These factors can be combined to examine the strain path angle, or the angle from the specimen's original rolling direction to its ultimate position in strain space, defined by the original rolling and transverse directions. This strain path angle sheds insight into the movement of R-value curves when subjected to various pre-straining and annealing conditions. Furthermore, the strain path diagram itself reveals the effect of pre-strain and annealing on the in-plane anisotropy of a specimen. The mechanisms of recovery and recrystallization can be seen in the strain path diagram based on the symmetry of the R-values about the diagonal (45 degree strain path) as a random texture would mostly eliminate the initial anisotropy of the material.

The texture evolution of the specimens due to pre-straining is corroborated by EBSD analysis, which shows strengthening of the brass texture due to equibiaxial pre-straining to 0.20. Thus, despite the planar isotropy of equibiaxial pre-straining, some amount of anisotropy remains in the material. Further EBSD analysis of annealed specimens will reveal the microstructural changes after this process.

REFERENCES

Hill. R., (1948), “A theory of the yielding and plastic flow of anisotropic metals,” Proc. Roy. Soc. London, 193, 281–297.

Hill. R., (1979), “Theoretical plasticity of textured aggregates,” Math. Proc. Camb. Phil. Soc., 85(1), 179–191.

Hu, L., Rollett, A.D., Iadicola, M., Foecke, T., Banovic, S., (2012), “Constitutive relations for AA 5754 based on crystal plasticity,” Metallurgical and Materials Transactions A, 43A, 854-869.

Huang, G., Yan, B., Z., Xia, (2011), “Measurement of R-values of high strength steels using digital image correlation,” SAE International Journal of Materials and Manufacturing, 4, 385-395.

Inoue, H., Takasugi, T., (2007), “Texture control for improving deep drawability in rolled and annealed aluminum alloy sheets,” Materials Transactions, 48, 2014-2022.

Kocks, U.F., Tomé, C.N., Wenk, H.-R., (2000), “Texture and Anisotropy: Preferred Orientations in Polycrystals and their Effect on Materials Properties,” Cambridge University Press, Cambridge, UK, 429-430.

Li, J. Kim, S., Lee, T. M., Krajewski, P. E., Wang, H., Hu, S. J., (2011), “The effect of pre-strain and subsequent annealing on the mechanical behavior of AA5182-O,” Materials Science and Engineering A, 582, 3905-3914.

Li, J., Carsley, J. E., Stoughton, T. B., Hector, Jr., L. G., Hu, S. J., (2013), “Forming Limit Analysis for Two-Stage Forming with Intermediate Annealing,” International Journal of Plasticity, 45, 21-43.

Liu, Y., Johnson, L. K., (1985), “Hill’s Plastic Strain Ratio of Sheet Metals,” Metallurgical Transactions A, 16A, 1531.

Liu, Y., Zhu, W., (1995), “Experimental investigation of the *r* and *Δr* value in A-K sheet subjected to two-stage straining,” Journal of Materials Processing Technology, 48, 129-133.

Lankford, W. T., Snyder, S. C., Bausher, J. A., (1950), “New criteria for predicting the press performance of deep drawing sheets,” Transactions of the American Society of Metals, 42, 1197–1205.

Rees, D. W. A., (1997), “A tensor function for the R-value of sheet metal,” Appl. Math. Modeling, 21, 579-590.

Transformation of strains by Mohr’s circle <http://www.efunda.com/formulae/solid_mechanics/mat_mechanics/mohr_circle_usage_strain.cfm>

Appendix 3.A Material Pre-strained in Equibiaxial tension to 0.20 without anneal (EB-20-0) R-values

Table 3.A R-values, denoted as R_h, as a function of testing direction measured from the rolling direction (RD) and as function of the strain path angle θ'.

Angle from RD (deg)	0	15	30	45	60	75	90
θ'	8.757	7.542	20.291	43.377	65.274	81.306	83.48
R_h	0.641	0.649	0.734	0.756	0.753	0.733	0.754

Appendix 3.B Material Pre-strained in Equibiaxial tension to 0.20 with 10 second anneal (EB-20-10) R-values

Table 3.B R-values, denoted as R_h, as a function of testing direction measured from the rolling direction (RD) and as function of the strain path angle θ'.

Angle from RD (deg)	0	15	30	45	60	75	90
θ'	-10.836	15.329	7.05	42.437	80.537	98.577	102.445
R_h	0.665	0.689	0.708	0.783	0.766	0.756	0.782

Appendix 3.C Material Pre-strained in Equibiaxial tension to 0.20 with 20 minute anneal (EB-20-0) R-values

Table 3.C R-values, denoted as R_h, as a function of testing direction measured from the rolling direction (RD) and as function of the strain path angle θ'.

Angle from RD (deg)	0	15	30	45	60	75	90
θ'	-22.428	-2.078	-8.143	41.37	108.644	113.387	113.413
R_h	0.748	0.773	0.817	0.865	0.835	0.823	0.804

Note: Strain Path Diagrams for Appendices 3.A-C were presented in Chapter 3.3

Appendix 3.D Material Pre-strained in Plane Strain to 0.20 without anneal (PS-20-0) R-values and Strain Path Diagrams

Table 3.D R-values, denoted as R_h, as a function of testing direction measured from the rolling direction (RD) and as function of the strain path angle θ'.

Angle from RD (deg)	0	15	30	45	60	75	90
θ'	8.757	7.542	20.291	43.377	65.274	81.306	83.48
R_h	0.641	0.649	0.734	0.756	0.753	0.733	0.754

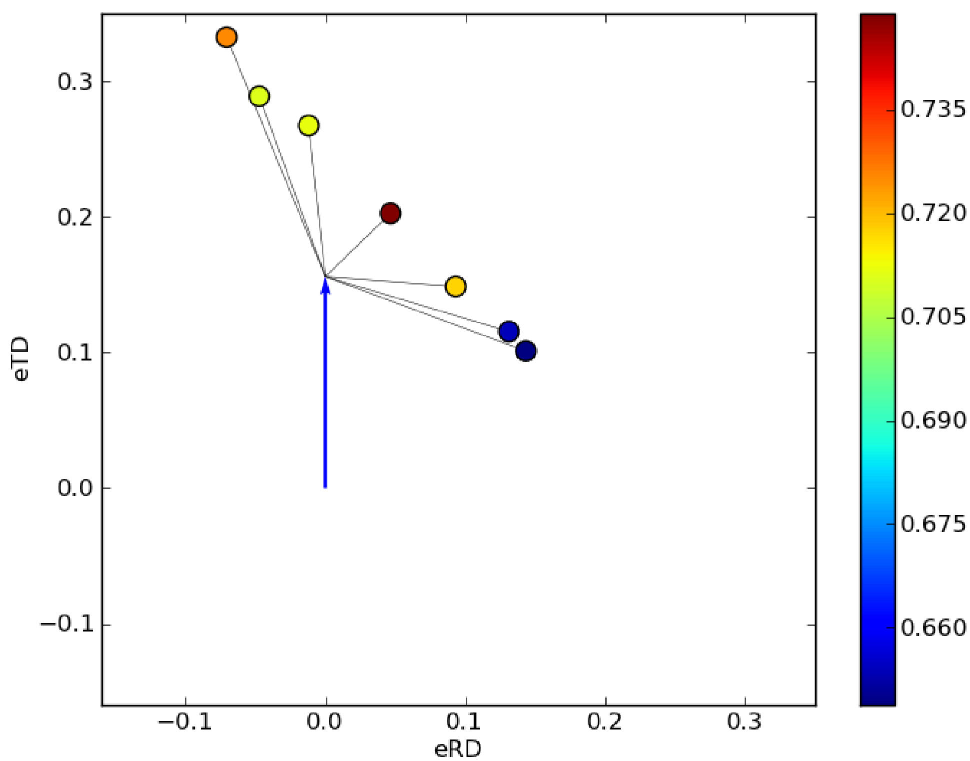

Figure 3.D PS-20-0 strain path taken in the pre-strain basis (defined by eRD and eTD). The blue arrow indicates the initial plane strain pre-straining step, starting at (eRD, eTD) = (0,0). The gray lines indicate the strain paths taken by individual uniaxial tension tests, with color indicating the final R-value.

Appendix 3.E Material Pre-strained in Plane Strain to 0.20 with 10 second anneal (PS-20-10) R-values and Strain Path Diagrams

Table 3.E R-values, denoted as R_h, as a function of testing direction measured from the rolling direction (RD) and as function of the strain path angle θ'.

Angle from RD (deg)	0	15	30	45	60	75	90
θ'	N/A	-11.386	15.772	69.547	97.815	103.181	N/A
R_h	N/A	0.697	0.721	0.802	0.754	0.702	N/A

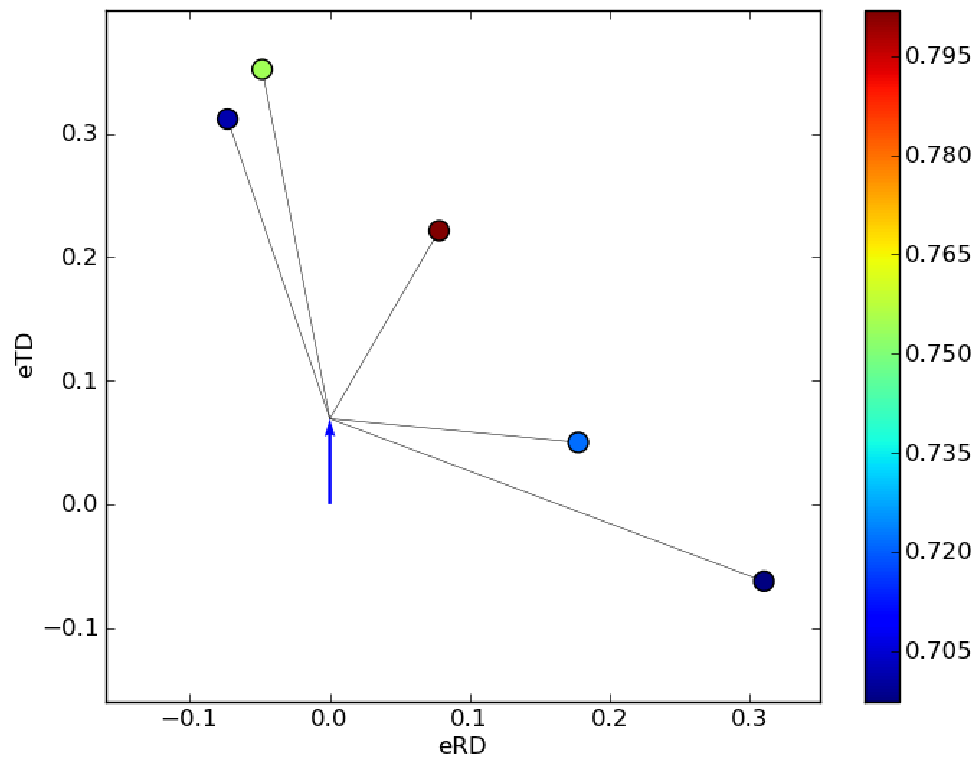

Figure 3.E PS-20-10 strain path taken in the pre-strain basis (defined by eRD and eTD). The blue arrow indicates the initial plane strain pre-straining step, starting at (eRD, eTD) = (0,0). The gray lines indicate the strain paths taken by individual uniaxial tension tests, with color indicating the final R-value.

Appendix 3.F Material Pre-strained in Plane Strain to 0.20 with 10 second anneal (PS-20-10) R-values and Strain Path Diagrams

Table 3.F R-values, denoted as R_h, as a function of testing direction measured from the rolling direction (RD) and as function of the strain path angle θ'.

Angle from RD (deg)	0	15	30	45	60	75	90
θ'	-27.025	-11.244	-10.404	83.905	96.964	100.978	116.136
R_h	0.697	0.815	0.883	0.96	0.902	0.716	0.549

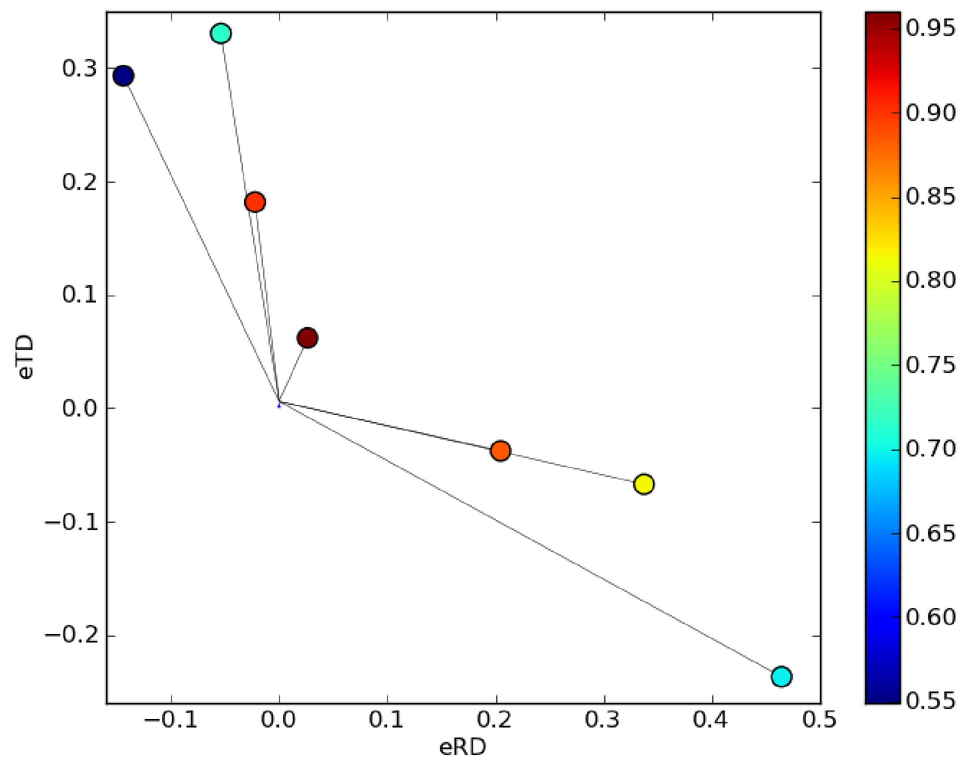

Figure 3.F PS-20-20 strain path taken in the pre-strain basis (defined by eRD and eTD). The blue arrow (which has a negative direction and very small magnitude due to the anneal) indicates the initial plane strain pre-straining step, starting at (eRD, eTD) = (0,0). The gray lines indicate the strain paths taken by individual uniaxial tension tests, with color indicating the final R-value.

Appendix 3.G Material Pre-strained in Uniaxial tension to 0.15 without anneal (UA-15-0) R-values and Strain Path Diagrams

Table 3.G R-values, denoted as R_h, as a function of testing direction measured from the rolling direction (RD) and as function of the strain path angle θ'.

Angle from RD (deg)	0	15	30	45	60	75	90
θ'	34.256	44.002	62.465	92.232	106.258	112.45	114.638
R_h	0.676	0.685	0.716	0.769	0.748	0.765	0.799

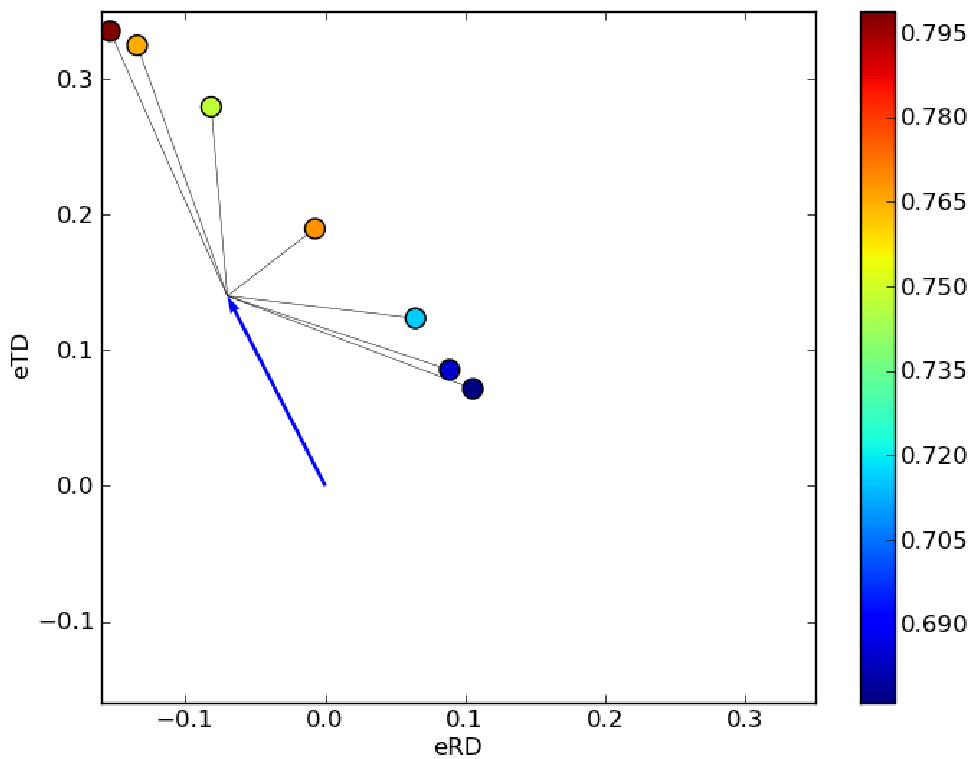

Figure 3.G UA-15-0 strain path taken in the pre-strain basis (defined by eRD and eTD). The blue arrow indicates the initial uniaxial pre-straining step, starting at (eRD, eTD) = (0,0). The gray lines indicate the strain paths taken by individual uniaxial tension tests, with color indicating the final R-value.

Appendix 3.H Material Pre-strained in Uniaxial tension to 0.20 with 20 minute anneal (UA-20-20) R-values and Strain Path Diagrams

Table 3.H R-values, denoted as R_h, as a function of testing direction measured from the rolling direction (RD) and as function of the strain path angle θ'.

Angle from RD (deg)	0	15	30	45	60	75	90
θ'	34.256	44.002	62.465	92.232	106.258	112.45	114.638
R_h	0.676	0.685	0.716	0.769	0.748	0.765	0.799

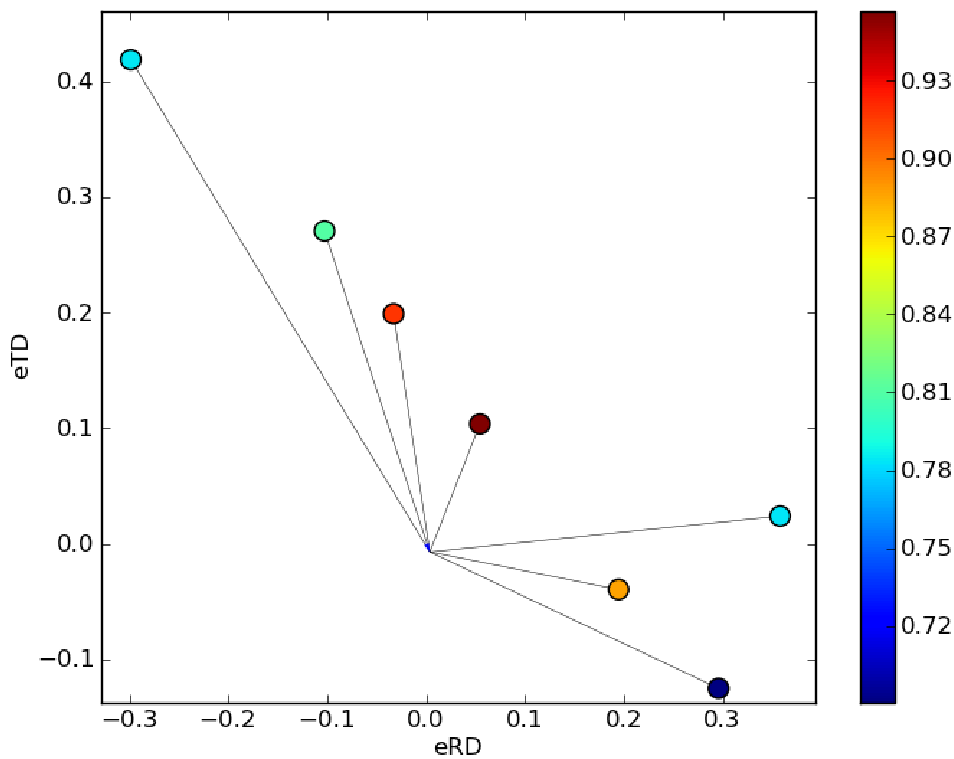

Figure 3.H UA-20-20 strain path taken in the pre-strain basis (defined by eRD and eTD). The blue arrow (which has a negative direction and very small magnitude due to the anneal) indicates the initial uniaxial pre-straining step, starting at (eRD, eTD) = (0,0). The gray lines indicate the strain paths taken by individual uniaxial tension tests, with color indicating the final R-value.

CHAPTER 4

CONCLUSIONS AND FUTURE WORK

It was observed that the Voce-Tangent model had the best overall fit of all the strain hardening laws considered. Due to the fact that it only introduced a weighting mechanism after the identification of the diffuse neck, the Voce-Tangent model provided a close fitting upper bound of the true stress-strain curve, enabling a more accurate prediction of the stress-state in this region than other models considered. However, it is important to validate these results with finite element methods (FEM) as ultimately, the goal of an improved strain hardening law is to extrapolate the stress state at large strains, close to 1.0. Because experimental detection of these strains is difficult, FEM simulations would provide additional evidence for the correctness of the proposed model. Indeed, current methods cannot consistently measure strains significantly greater than 0.30.

Furthermore, the strain path, which incorporates the effect of pre-strain, annealing, and the uniaxial testing direction of a specimen, is a useful parameter in predicting the anisotropy of the material. This is because the strain paths, as well as the strain-path angle, provide a more detailed summary of the deformation of a material than merely the equivalent plastic strain; consequently, the changes in material anisotropy can be predicted even after a variety of process conditions. However, the R-value, which captures the anisotropy of a material, did not always have a simple correlation with the strain path of a given specimen. EBSD as a material analysis method gives insight information on texture evolution, which will be helpful to explain the macro anisotropic behavior and thus is important to this research. Since EBSD data was only available for a subset of the specimens considered, namely, specimens pre-strained equibiaxially without annealing, it would be useful to have microstructural data for the remaining specimens to explain the effects of pre-strain and annealing that are not captured by the strain-path diagram, in which all the process conditions are captured by a two-dimensional displacement in strain-space.